HYDROGEN DIFFUSION AND TRAPPING IN ELECTRODEPOSITED NICKEL

by

THOMAS MILLER HARRIS

B.S., Butler University (1979)
M.S., Massachusetts Institute of Technology (1987)

Submitted to the Department of Materials Science and Engineering
in partial fulfillment of the requirements for the degree of

DOCTOR OF PHILOSOPHY

at the

MASSACHUSETTS INSTITUTE OF TECHNOLOGY

September, 1989

Signature of Author_____
Department of Materials Science and Engineering, August 11, 1989

Certified by_____
Professor Ronald M. Latanision, Thesis Supervisor

Accepted by_____
Professor Linn W. Hobbs, Chairman,
Departmental Committee on Graduate Students

HYDROGEN DIFFUSION AND TRAPPING IN ELECTRODEPOSITED NICKEL

by

Thomas Miller Harris

Submitted to the Department of Materials Science and Engineering
on August 11, 1989 in partial fulfillment of the requirements
for the degree of Doctor of Philosophy

Abstract

In an attempt to quantify grain boundary diffusion of hydrogen in nickel, permeation in electrodeposited foil has been investigated. Pinhole-free specimens were plated from a nickel sulfamate bath onto a reusable anodized titanium cathode. The microstructure was a mixture of regions of fine grains (diameters <0.1 μm) and individual grains up to 2 μm in diameter. The specimens were subjected to several heat treatments that resulted in grain growth; at lower temperatures, the growth was limited primarily to the fine-grained regions. At higher temperatures, second phase particles formed throughout the nickel.

Electrochemical boundary conditions were used to produce permeation. The effective diffusion coefficient was determined from the transient in the permeation current density. With the electrodeposited nickel, this value was found to decrease with an increase in the initial concentration of hydrogen in the specimen. This behavior indicates the presence of hydrogen trap sites in the material.

The effective diffusion coefficient measured with fully annealed specimens was in agreement with previously-reported values of the lattice diffusion coefficient (7.8×10^{-14} m^2/s at 30 °C). This suggests that trapping has a negligible effect on diffusion in this material. Thus, the relationship between the input hydrogen concentration (C_o) and the cathodic current density applied to the input surface (i_c) could be determined through Fick's First Law.

Assuming that the relationship between C_o and i_c is also valid for the electrodeposited nickel, the true diffusion coefficient (which is unaffected by trapping) can be determined from the

steady state permeation current density. This value averaged 3.3 x 10^{-12} m^2/s at 30 °C. Analysis of the diffusion data using the Hart model suggests that the experimentally determined true diffusion coefficient is a good approximation of the grain boundary diffusion coefficient at 30°C.

The activation energy for diffusion of hydrogen in the electrodeposited nickel, determined from an Arrhenius plot of experimental data collected over the temperature range 22-72°C, was 14 kJ/mol. When the least-squares fit of this data was forced through the y-axis intercept (D_0) for lattice diffusion of hydrogen (as suggested by Zener), the activation energy was 30 kJ/mol. This last value is only slightly lower than that for grain boundary diffusion of hydrogen in nickel determined in a previous study, and 75% of that for lattice diffusion. The Hart model suggests that the lower value determined without the use of D_0 results from the effect of temperature on trapping of hydrogen at grain boundary trap sites, which can enhance grain boundary diffusion.

Analysis of the permeation data from the electrodeposited nickel using the McNabb-Foster model provided a trap binding energy of 29 kJ/mol and a trap site density of 4 x 10^{18} cm^{-3}. The former value is nearly three times larger than the grain boundary binding energy determined in high-purity, well-annealed nickel, but approximately equal to that for binding energy to incoherent phase boundaries surrounding oxide particles. The latter value is slightly larger than the bulk oxygen concentration of the electrodeposited nickel. Thus, it appears that, with respect to the McNabb-Foster model, hydrogen trapping at "clean" grain boundaries is obscured by stronger trapping at oxygen atoms or very small second phase particles.

The results above suggest that grain boundary diffusion of hydrogen in nickel is not fast enough to allow hydrogen to penetrate well ahead of the advancing tip of an hydrogen-induced crack. Thus, hydrogen transport in the plastic zone surrounding the crack tip, which can occur by dislocation transport as well as grain boundary diffusion, would appear to control the rate of crack advance.

Thesis Supervisor: Ronald M. Latanision
Professor of Materials Science and Engineering

Table of Contents

Acknowledgements

The financial support of the Shell Companies Foundation is gratefully acknowledged. The anodized titanium cathodes were supplied by Dr. Jean-Luc Delplanke, a Belgium scientist who paid a timely visit to our lab. Mr. Mike Frongillo assisted with the TEM examinations and interpretation.

I have been privileged to interact with two professors whom I hope to emulate in my academic career. Professors Robert Balluffi and Herbert Uhlig constantly amazed me with their breadth of knowledge, and their willingness to take the time to share it with students.

Three student friendships have been very important to me. I met Tresa Pollock, Tom Moffat and Pat McCann the week before classes began five years ago. No doubt much of this bond can be attributed to identical trials and tribulations, but their is a common thread to our thoughts that has provided many hours of stimulating conversation.

Finally, I would like to thank Cindy, my wife, for her support through what has no doubt been a greater ordeal for her than for me. We are both looking forward to a new phase of our lives.

1. Introduction

Nickel and nickel-based alloys exhibit excellent resistance to corrosion and are used extensively in corrosive environments. In acidic media, these materials can exhibit a loss in ductility, particularly when coupled to a more active metal. These observations suggest that hydrogen, the product of the cathodic half-reaction that is promoted through galvanic coupling, is responsible for the embrittlement, or at least contributes to it.

The hydrogen-induced reduction of ductility is accompanied by a change in fracture mode from ductile rupture to intergranular. Thus, hydrogen localizes the breaking of nickel-nickel bonds to the grain boundaries. One explanation for this behavior is that solute hydrogen weakens metallic bonding, and that segregation produces a much higher concentration of hydrogen at the grain boundaries than in the adjacent grains. While the first statement has yet to be established unambiguously, the role of segregation was clearly demonstrated in a recent study by Lassila and Birnbaum (1). Nickel was not embrittled by a uniform distribution of hydrogen. When the hydrogen segregated to the grain boundaries, intergranular fracture was observed.

The work of Lassila and Birnbaum suggests that the kinetics of the accumulation of hydrogen at the grain boundaries may serve to describe the kinetics of the overall embrittlement process. In the case of solute hydrogen (i.e., already dissolved in the material, as in the experiments above), the process of accumulation involves only segregation. When the source of hydrogen is external to the material, the accumulation process may be divided into three parts:

1. absorption of hydrogen from the environment,
2. transport of hydrogen from the surface to the interior,

3. segregation of hydrogen to the grain boundaries.

Since the rate of hydrogen diffusion in nickel is relatively slow, the second step is usually the rate-limiting process.

Hydrogen-induced sub-critical crack growth rates have been shown to be similar for iron and nickel (2). Since the rate of lattice diffusion of hydrogen in these metals is vastly different, it has been suggested that other transport processes may be important. The mechanism receiving the most attention to date is known as dislocation transport: hydrogen, segregated to a dislocation, is dragged along when the dislocation moves. While dislocation transport in nickel has been detected under a limited set of circumstances (4,5), other conditions (3,5) have been found to promote a related process known as dynamic trapping, in which the overall penetration of hydrogen (from an external source) is reduced by trapping at dislocations nucleated during plastic straining.

Enhanced transport may also occur by short-circuit diffusion associated with crystalline defects. Several studies suggest that grain boundary diffusion of hydrogen is more rapid than lattice diffusion in nickel at room temperature; however, quantitative results are limited. Mutschele and Kirchheim (6) have quantified grain boundary diffusion in palladium by comparing hydrogen transport in single crystal and fine-grained specimens. The fine-grained material exhibited an average grain diameter of 12 nm, which corresponds to a grain boundary volume fraction of 0.5; thus, grain boundaries dominate the transport of hydrogen in this material. The results of the study are presented in Fig. 1. The diffusion coefficient determined with the single crystal (D_l) was independent of hydrogen concentration, and was in agreement with the results of previous studies of lattice diffusion in palladium. At low hydrogen concentrations, the diffusion coefficient determined with the fine-grained material

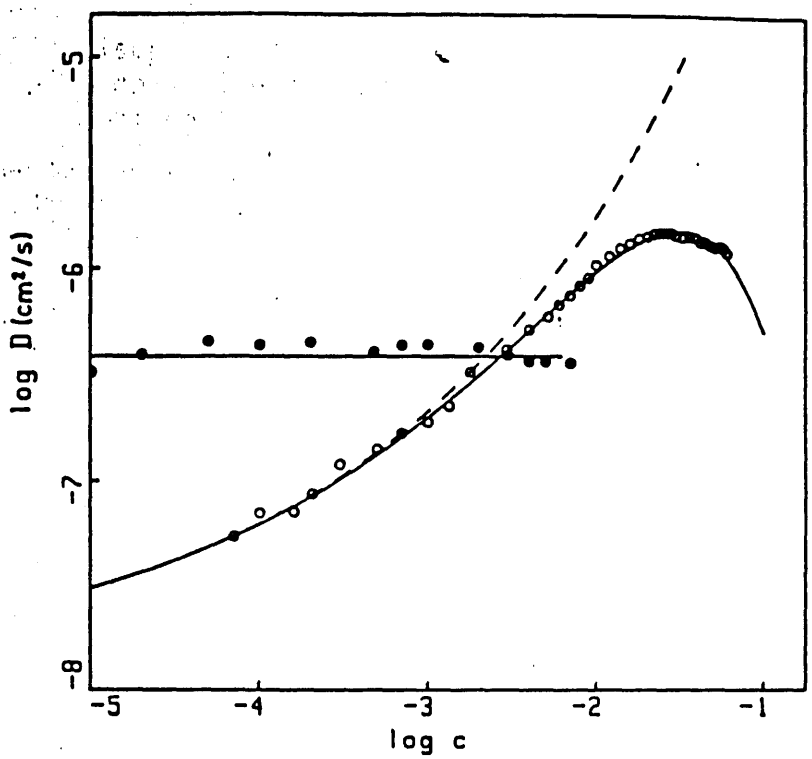

Fig. 1. Effect of hydrogen content on the effective diffusion coefficient at 30°C for palladium single crystal (solid circles) and nanocrystalline (open circles) specimens. (Ref. 6)

was ten times smaller than D_l. With increasing hydrogen content, the diffusion coefficient increased by nearly two orders of magnitude.

The concentration-dependence of hydrogen diffusion in the fine-grained palladium is a manifestation of grain boundary segregation. As hydrogen is known to segregate to grain boundaries in nickel, this phenomenon was considered in the present study of grain boundary diffusion of hydrogen in nickel.

The work of Mutschele and Kirchheim also indicates that grain boundary diffusion can be quantified through conventional hydrogen transport measurements, provided that the test specimens contain a sufficient number of grain boundaries. Both Archer and Grant (7) and Rommal and Moran (8) have noted rapid hydrogen permeation in electrodeposited nickel. Thus, the present study utilized permeation measurements on electrodeposited nickel foils to estimate the grain boundary diffusion coefficient.

2.0. Literature Survey

Studies of grain boundary phenomena can be separated into two groups: microscopic and macroscopic. The former involve only a few grain boundaries, or in some cases, only one (i.e., a bicrystal specimen). Microscopic studies are useful in demonstrating, for instance, that grain boundary structure can affect hydrogen diffusion. However, determination of a representative value of the grain boundary diffusion coefficient will require many microscopic measurements. In contrast, a macroscopic measurement samples the behavior of many grain boundaries simultaneously, thus providing an "average" value in a single test. The disadvantage of the macroscopic approach is that the behavior being measured cannot be unambiguously attributed to the grain boundaries. The distinction between a microscopic and macroscopic method is important to the assessment of previous studies of grain boundary diffusion of hydrogen in nickel.

2.1. Grain Boundary Diffusion of Hydrogen

Three microscopic methods for studying the grain boundary diffusion of hydrogen in nickel have been reported. Schober and Dieker (9) have described a chemical technique purported to detect localized hydrogen fluxes at grain boundaries. The specimens were electropolished, cathodically charged with hydrogen and then exposed to a silver cyanide solution. This treatment resulted in the formation of particles primarily along grain boundaries intersecting the specimen surface. It was assumed that the particles were silver metal, produced by a redox reaction between the silver cyanide complex and hydrogen emanating from the grain boundaries. Tseng et al (10) have extended this technique to the detection of hydrogen permeating through a thin nickel foil. In commenting on the paper by Tseng et al, Harris and Latanision (11) noted that 1) the composition of the solution specified by Schober and Dieker

allows silver cyanide compound to homogeneously precipitate in the presence of any other cation that complexes with cyanide ion (e.g. hydrogen ion), 2) both silver cyanide compound and the particles deposited from the test solution are soluble in dilute sodium cyanide solution, whereas silver electrodeposited on nickel is not, and 3) the electron diffraction patterns of the particles do not match those of silver metal. These results suggest that the particles are silver cyanide compound rather than silver metal. Thus, the usefulness of this technique for studying grain boundary diffusion of hydrogen is questionable.

Tsuru and Latanision (12) have used a secondary ion mass spectrometer (SIMS) to detect hydrogen permeating through a nickel foil; this technique provides spatial resolution on the order of 10 μm. Hydrogen was cathodically charged into one surface of the foil specimen for a period of time presumably too short to allow hydrogen to permeate through the specimen by lattice diffusion. Line scans across the other surface revealed higher concentrations of hydrogen in the vicinity of the grain boundaries relative to intragranular regions. It was concluded that the higher concentrations arose through enhanced permeation along the grain boundaries.

Ladna and Birnbaum (13) have use SIMS to profile the deuterium concentration in nickel bicrystals having symmetric tilt boundaries with <110> rotation axes. The deuterium was cathodically charged at room temperature into a surface perpendicular to the plane of the interface. The specimen was cooled to 195 K in the vacuum chamber of the instrument in order to limit the redistribution of deuterium during analysis. Enhanced penetration of deuterium along the grain boundary (relative to the adjacent perfect crystals) was reported for specimens with a 39° symmetric tilt boundary ($\Sigma = 9$), which possesses a high interfacial energy. A 129° boundary ($\Sigma = 11$), which is representative of a low-energy interface, did not exhibit enhanced penetration. A direct correlation between enhanced diffusion and interfacial

energy has been observed in other systems (14).

In the experiments above, the cathodic current density was sufficient to produce a layer of deuteride layer across the entire surface. The enhanced penetration of deuterium along the $\Sigma = 9$ boundary was in the form of enhanced growth of deuteride in this region. Ladna and Birnbaum noted that the extent to which the deuteride grew into the perfect crystals adjacent to the grain boundary was approximately thirty times less than that predicted by assuming that the diffusion of deuterium in α-nickel is the rate-limiting process. Thus, they concluded that diffusion of deuterium in the deuteride layer was the slow step. Regardless of whether this conclusion is valid or not (hydrogen diffusion in palladium hydride is thirty times faster than in α-palladium (15)), it is clear that the enhanced growth of deuteride along the $\Sigma = 9$ grain boundary is not controlled by the diffusion of deuterium ahead of the phase boundary. Thus, this experiment indicates that grain boundary structure can influence the formation of deuteride, but does not demonstrate that deuterium diffuses more rapidly in grain boundaries than in a perfect crystal.

As noted in the introduction, the fracture morphology of nickel changes when a sufficient concentration of hydrogen is segregated to the grain boundaries. Kimura and Birnbaum (16,17) have made use of this characteristic to detect grain boundary diffusion. High-purity wire specimens were cathodically charged at room temperature, and then fractured in liquid nitrogen. When hydrogen was not introduced into the specimen, the fracture was completely ductile. With increasing time of cathodic charging, the extent of intergranular fracture (IGF), which initiated at the surface, increased. Thus, the extent of IGF could be used to estimate the the depth of penetration of hydrogen during charging (the liquid nitrogen provides a temperature sufficiently low to limit the redistribution of hydrogen during the tensile test). The concentration of hydrogen required for intergranular fracture was found at a greater depth

than that predicted by the appropriate solution to Fick's Second Law and the lattice diffusion coefficient for hydrogen in nickel. Grain boundary diffusion during the charging at room temperature was invoked to explain the discrepancy.

Kimura and Birnbaum analyzed the results in order to determine an absolute value for the grain boundary diffusion coefficient. Yao and Cahoon (18) have identified several errors in the derivation of this analysis which cast doubt upon the diffusion coefficient value. However, neither the authors nor their critics recognized the most objectionable features of this method. First, it too is microscopic in nature. The average grain diameter of the test material was 80 μm, and the average specimen diameter was 250 μm; therefore, the average crack path involved only four or five grain boundaries. It is unlikely that this small number of grain boundaries is representative of the average grain boundary in terms of the diffusion of hydrogen, or even the micromechanics of hydrogen-induced fracture, upon which the measurement of hydrogen penetration is based.

The use of well-annealed nickel by Kimura and Birnbaum may also be misleading. The effect of annealing on grain boundary structure in copper and silver has been studied by Herrmann et al (19). Thousands of single crystal balls approximately 100 μm in diameter were sintered onto a single crystal plate. The orientation of the balls with respect to the plate, which was monitored by x-ray diffraction, was initially random. However, with continued annealing many of the balls rotated to reduce the energy of the grain boundary that forms between each ball and the plate. After many hours of annealing, virtually all of the balls had rotated into orientations corresponding to "special" grain boundaries exhibiting low interfacial energies. Although grain rotation in a polycrystalline nickel specimen is more constrained than in the experiments above, many of the high-energy grain boundaries, which are believed to be the pathways of least resistance for hydrogen diffusion, will be eliminated by annealing. Thus, grain boundary diffusion measurements conducted on well-annealed nickel may not accurately

reflect this phenomenon over the full range of grain boundary structures.

Attempts to measure grain boundary diffusion macroscopically have met with mixed success. Robertson (20) found no evidence for grain boundary diffusion in gas-phase permeation measurements, but the smallest grain size examined was 30 μm. Louthan et al (21) noted that permeation through severely cold-worked nickel was approximately two times greater than that measured after the material was annealed. They attributed the extra flux to short-circuit diffusion through dislocations, which were arranged in cells approximately 0.3 μm in diameter. However, the temperature dependence of the permeability was the same in both materials (Fig. 2); true short-circuit diffusion would be expected to exhibit a reduced slope, relative to lattice diffusion, in an Arrhenius plot.

Tsuru and Latanision (12) have used the electrochemical permeation technique (described in detail in section 4.2) to detect grain boundary diffusion of hydrogen in nickel. With well-annealed nickel, a two-stage transient in the flux was observed (Fig. 3). Analysis of the second stage provided a diffusion coefficient which was consistent with the results of previous studies of lattice diffusion. Analysis of the first stage, which was much smaller in magnitude than the second, suggested that the corresponding diffusion coefficient was sixty times greater than the lattice diffusion coefficient. The first stage of the transient was attributed to grain boundary diffusion of hydrogen.

The primary criticism of the permeation measurements of Tsuru and Latanision involves the absolute sensitivity of the detection of hydrogen fluxes through a thin nickel foil. The "steady-state" permeation current density of the first stage of the transient was on the order of 2 nA/cm^2. This signal was measured on top of a background current density, resulting from oxidation of the nickel surface, of greater than 10 nA/cm^2. A small increase in the temperature

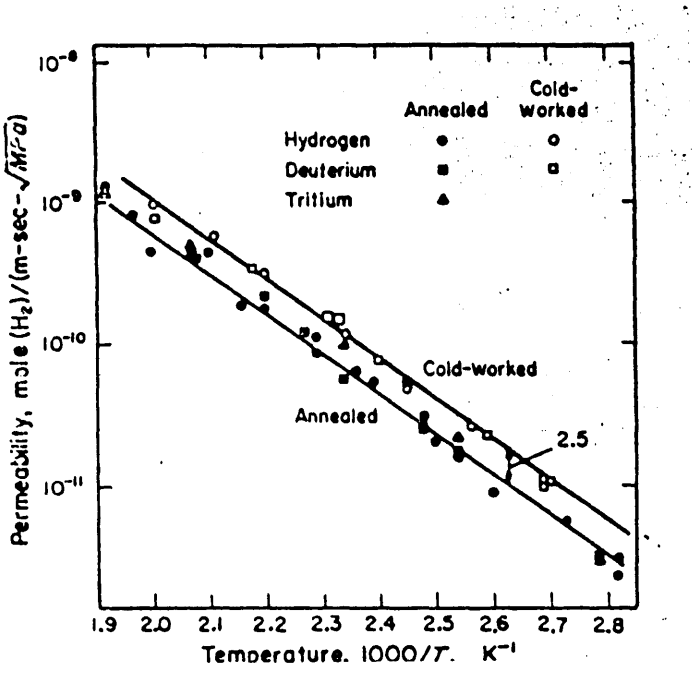

Fig. 2. Temperature dependence of hydrogen, deuterium and tritium permeability in cold-worked and annealed nickel. (Ref. 21)

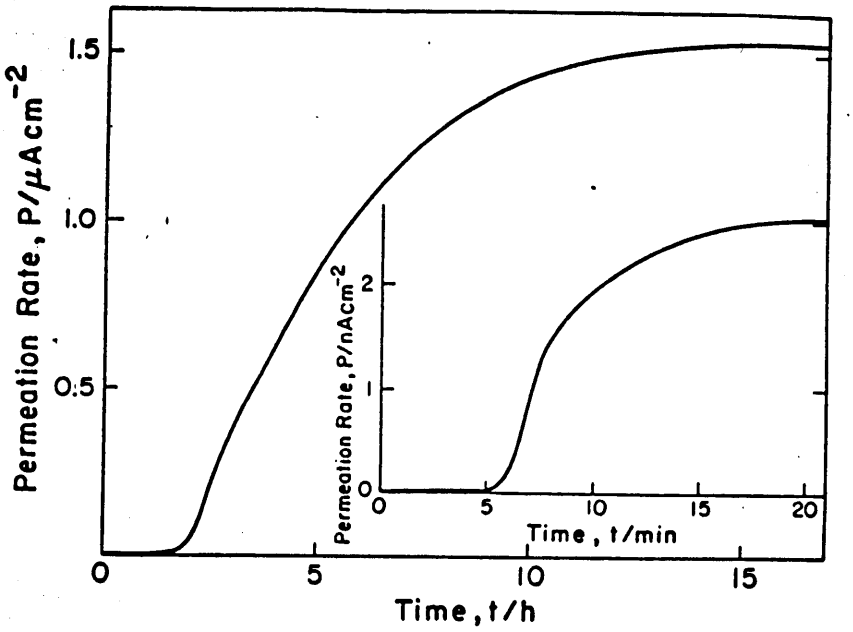

Fig. 3. Two-stage transient in the hydrogen permeation current density measured with annealed nickel at 25 °C. (Ref. 12)

of the foil can easily produce a rise in the background current density exceeding 2 nA/cm^2 (22). However, it is conceivable that this problem could be overcome through the use of fine-grained specimens.

2.2. Segregation (Trapping) of Hydrogen at Grain Boundaries

As noted in the introduction, segregation can affect grain boundary diffusion. The sites in the grain boundary to which hydrogen segregates are known as traps. Atomistically, a trap is defined as a site for which the probability of hydrogen jumping in (capture) is greater than that for hydrogen jumping out (escape). The probability of capture is increased by a decrease in the chemical potential of the site relative to a perfect lattice site (an octahedral interstice). The probability of escape is reduced by the presence of a greater activation barrier than that encountered for a jump between adjacent perfect lattice sites. These factors are illustrated in Fig. 4.

Trapping has not been considered in studies of grain boundary diffusion in nickel. However, the phenomenon has been investigated as a separate process. The microscopic approach has provided unambiguous proof that hydrogen can be trapped at grain boundaries in nickel. Using SIMS, Fukushima and Birnbaum (23) analyzed individual grain boundaries in polycrystalline nickel for deuterium enrichment (relative to intragranular regions). Specimens were equilibrated with 100 kPa $^2H_2$ at 1500 K, and quenched in silicone oil; this treatment provided an overall deuterium content of 500 appm. Deuterium segregation to the grain boundaries was not detected until the specimens were aged (in the vaccum chamber of the SIMS) for several hours at 245 or 295 K. Deuterium was not trapped to all boundaries, suggesting that grain boundary structure also plays a role in this phenomenon.

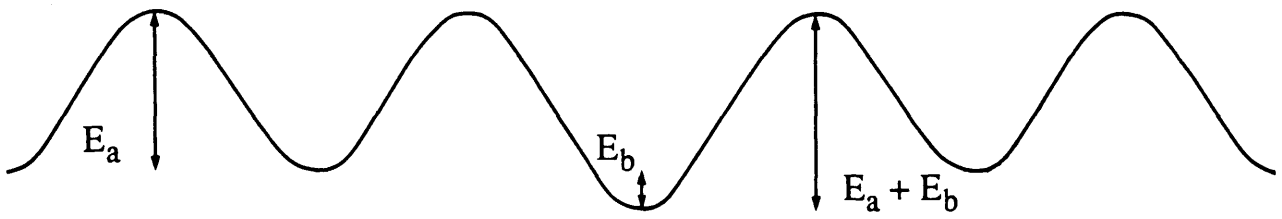

Fig. 4. Energy model for grain boundary trap site in nickel. E_a is activation energy for lattice diffusion. E_b is binding energy for trap site.

Since the depth resolution of SIMS is much better than its lateral resolution, Fukushima and Birnbaum analyzed material near the surface to quantify the segregation of deuterium. Aging at 245 K for several hours provided a deuterium concentration which was nearly 100 times greater than the bulk concentration. Interestingly, this segregation was observed to extend well beneath the surface, prompting the authors to conclude that the segregation of deuterium to interfaces is "non-classical" (i.e., different from the behavior of all other alloys that have been examined). However, this behavior could also result from heating of the specimen (which was supposedly maintained at 195 K throughout the analysis) due to sputtering, or trapping at dislocations near the surface produced by thermal stress associated with the severe quench.

As noted in the introduction, Lassila and Birnbaum (1) have used the characteristic change in fracture mode to quantify the trapping of hydrogen at grain boundaries. High-purity nickel tensile specimens were charged with hydrogen from mixtures of hydrogen and argon at 1425 K, quenched in water and stored in liquid nitrogen. Tensile testing (also in liquid N_2) of the specimens following this treatment resulted in completely ductile fracture, presumably as the result of a homogeneous distribution of hydrogen. Aging treatments at temperatures from 208-318 K and for times up to ten days allowed the hydrogen to segregate to the grain boundaries and produce intergranular fracture. The extent of IGF increased with increasing bulk hydrogen content and aging time (Fig.5). As the temperature of the aging treatment was increased, an increase in bulk hydrogen content was required to produce the same extent of intergranular fracture. These relationships are consistent with classical segregation behavior. An Arrhenius plot of the bulk hydrogen content required to produce a particular fraction of IGF provided an activation enthalpy of 11.6 kJ/mol.

The experiments of Lassila and Birnbaum (1) are also microscopic in nature. The dimensions of the tensile specimens and the large grain size produced by annealing were such that less

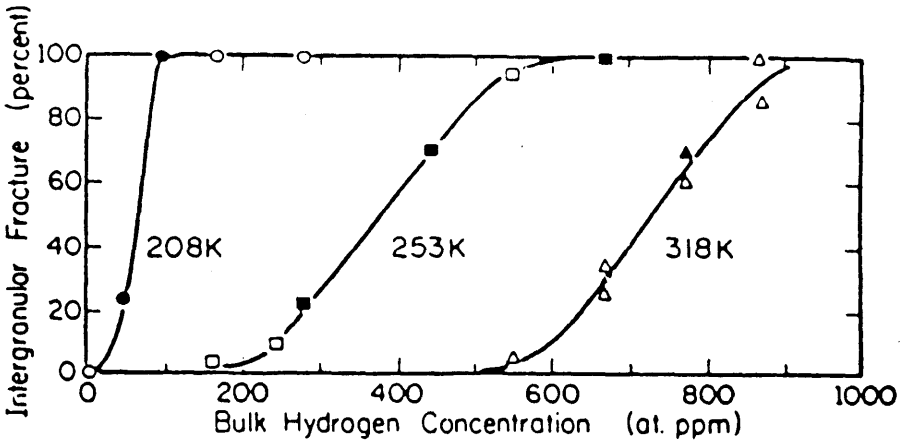

Fig. 5. Effect of total hydrogen concentration and aging temperature on the extent of intergranular fracture in nickel tensile specimens fractured in liquid nitrogen. Aging time was sufficient to ensure equilbrium segregation. (Ref. 1)

than 10 grain boundaries were involved in each measurement. The use of well-annealed material is also unfortunate; it is expected that trapping at "special" boundaries will be less than that associated with general grain boundaries.

The macroscopic approach has been much less successful in quantifying hydrogen trapping at grain boundaries. A reduction in the grain size has been shown to enhance the solubility of hydrogen in two studies (24,25), but not in a third (20). In one case (25), the binding energy to the grain boundary trap sites was determined to be 20.5 kJ/mol. However, the nickel specimens were only 99.97% pure, and had been annealed at temperatures between 800 and 1150 °C. Latanision and Operhauser (26) have shown that this same material (Ni270) is increasingly susceptible to hydrogen embrittlement with annealing at these temperatures. Analysis of the intergranular fracture surfaces by Auger electron spectroscopy revealed tin and antimony segregated to the grain boundaries. These impurities may enhance the segregation of hydrogen to the grain boundaries through solute-solute interactions.

Latanision and Operhauser also noted that the grain boundary impurity concentrations increased with increasing grain size. Thus, grain growth will result in the concentration of segregating impurities at those grain boundaries that remain. Even a high-purity material will exhibit contaminated grain boundaries after sufficient annealing. Atomistic computer simulations of hydrogen trapping at symmetric tilt boundaries representative of a wide range of grain boundaries in nickel have indicated that no site corresponds to a binding energy for hydrogen greater than 5 kJ/mol (27). Therefore, it would appear that the results of Lassila and Birnbaum (1) may also be affected by grain boundary impurities.

3. Research Objectives

It can be concluded from the previous section that while grain boundary diffusion of hydrogen in nickel has been demonstrated qualitatively, a quantitative understanding is lacking. Specifically, values for the activation energy and the room-temperature diffusion coefficient in the regime of trap saturation are needed. These parameters should be accessible through macroscopic measurements, provided the test material contains a sufficient number of grain boundaries.

Due to its successful application to the study of lattice diffusion of hydrogen in nickel (28-30, 7), the electrochemical permeation technique was chosen to quantify hydrogen transport in the present investigation. The production of hydrogen permeation with electrochemical boundary conditions has two distinct advantages, and two minor disadvantages. Establishing the low-concentration condition potentiostatically provides a sensitive measure of the hydrogen flux with relatively inexpensive equipment. Cathodic polarization of the other surface can readily produce hydrogen concentrations that cannot be practically obtained with hydrogen gas pressure; high pressures can plastically deform the specimen (thus initiating dynamic trapping) or, at the very least, introduce elastic stresses that influence permeation (31). One disadvantage of electrochemical boundary conditions is the limited temperature range over which routine measurements (i.e., not requiring a pressurized cell, nor a non-aqueous electrolyte that freezes well below 0°C) can be made. The other is that the zero concentration initial condition is difficult to reestablish following a permeation experiment. Thus, a different type of initial condition must be employed if multiple experiments are to be performed on a single specimen.

Hydrogen trapping can also be quantified with the electrochemical permeation technique. A

wide range of input concentrations can be produced by cathodic polarization. The initial hydrogen content can also be varied. The effect of these parameters on permeation can be analyzed with a generalized method developed by McNabb and Foster (32) to quantify the trapping of hydrogen at any type of crystalline defect. This analysis typically provides an estimate of both the binding energy of the trap site, and the number of sites with binding energies near this value.

As noted above, the nickel in which grain boundary diffusion of hydrogen is to be quantified must be fine-grained. This condition should provide both a wide range of grain boundary structures and low concentrations of segregating impurities at the grain boundaries. As noted above, rapid hydrogen diffusion has been observed in commercial electroplated foil (7,8). Although the microstructures of the materials used in these investigations were not reported, they were undoubtedly fine-grained. However, commercial nickel plate is usually contaminated with sulfur from organosulfur compounds added to the electrolyte to enhance the brightness of the deposit.

Thompson and Saxton (33) have described an electroplating process that provides relatively-pure nickel with a uniform grain size of 0.12 μm. The material also exhibited grain growth, rather than recrystallization, with annealing. Thus, this process had the potential to provide a material in which the average grain size could be varied over two orders of magnitude, so that the effect of grain size on both the diffusion and trapping of hydrogen in nickel could be studied.

4. Experimental Procedures

4.1. Specimen Preparation

As noted in the previous section, relatively pure, fine-grained nickel can be electrodeposited from an bath based on the sulfamate salt of nickel (33). Initial use of this electrolyte provided several usable permeation specimens. Therefore, this method was developed for the routine production of nickel foil.

The composition of the bath and the operating conditions that were used in this study are listed in Table 1. Analytical-grade reagents and distilled water (18 MΩ/cm conductivity) were used in its preparation. With two exceptions, these parameters were previously identified as providing smooth deposits with low internal stress. Fanner and Hammond (34) found that only 3.3 g/L of the chloride salt inhibited the passivation of a "depolarized" nickel anode. Sulfur is retained in this material to promote active dissolution (thus maintaining the nickel ion concentration in the electrolyte). Cold-rolled Ni270, which contains less than 5 ppm sulfur, was used as the anode material in the present study. In order to prevent this material from passivating, the addition of 20 g/L of $NiCl_2 \cdot 6H_2O$ was required.

As noted by Fanner and Hammond, a wetting agent must be added to prevent "pitting", which results from the adherence of bubbles of hydrogen gas (codeposited, in small amounts, with the nickel) to the deposit surface. A scanning electron micrograph of a pitted surface is presented in Fig. 6. Pits cannot be tolerated in a permeation specimen; they represent thin spots through which hydrogen can permeate more rapidly than through the rest of the specimen. Sodium dodecyl sulfate, at a concentration of only 0.1 g/L, was found to prevent hydrogen bubble adherence over most of the surface of the electrodeposit. Bubbles continued

Table 1.

Nickel electroplating bath composition and operating conditions.

Bath composition:

nickel sulfamate tetrahydrate.....350 g/L

boric acid..... 30 g/L

nickel chloride hexahydrate..... 20 g/L

dodecyl sulfate, sodium salt..... 0.1 g/L

Conditions:

pH.....4.0

anode.....Ni 270

cathode.....anodized titanium

cathode current density..... 500 A/cm^2

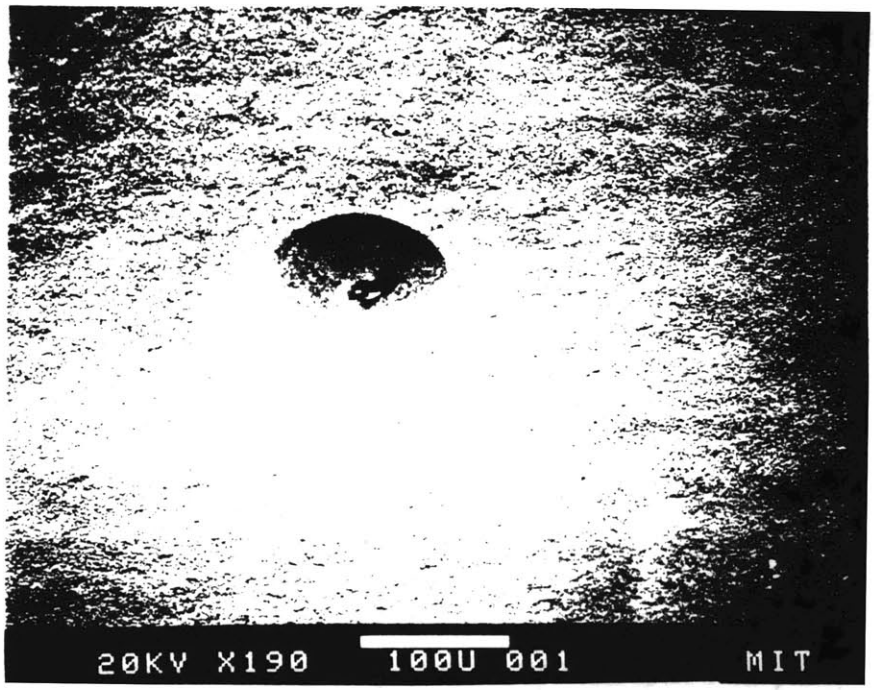

Fig. 6. Pit in nickel electrodeposit produced by adherent hydrogen bubble.

to form near the edges; they were removed periodically by flushing with electrolyte.

The internal stress of deposits from the sulfamate bath was sufficiently low to allow the use of an anodized titanium cathode, to which the nickel bonds physically but not chemically. Thus, following deposition of the desired amount of material, the specimen was simply peeled off the cathode surface. Deposits less than 15 μm thick were difficult to remove from the substrate in one piece. To avoid pinholes in the deposits (see section 6.1), several specimens were prepared in succession, with the substrate being returned to the electrolyte immediately following removal of the previous deposit.

The unused portions of the cathode surface were masked with clear, colorless Cutex nail polish. The codeposited hydrogen blistered this lacquer, requiring its replacement after the preparation of several specimens. Prior to remasking, the damaged coating was removed by soaking in acetone, followed by rinsing in high-purity ethanol, then distilled water.

Specimens were deposited in an open Pyrex beaker placed upon a hot plate, which regulated the temperature to 50±1 °C. The electrodes, both in the form of a strip approximately 3 cm in width, were placed in parallel approximately 3 cm apart. The surface area of the anode was approximately four times greater than that of the cathode (the unmasked portion), but one half of this area faced away from the cathode.

Changes occurred in the bath over time. Evaporation required the addition of distilled water at least every 1.5 hrs. After 3 A·hr of use, the bath was filtered through analytical-grade paper (S & S #589), and the pH was readjusted to 4.0. The wetting agent was also replenished after each filtration. Dendritic growth along the edges of the specimen was observed after 9 A·hr. As this behavior could not be remedied, the bath was discarded at his point.

The thickness (L) of the rectangular specimens was calculated with the expression:

$$L = \frac{m}{\rho \cdot a} \qquad [1]$$

where m = mass
ρ = bulk density of nickel
a = area defined by the length and width of the foil.

This method was found to provide thicknesses comparable to the metallographic examination of edge-mounted foils (35), validating the assumption of no porosity in the calculation above. Metallographic examination also indicated that the thickness was uniform throughout the specimen.

The electrodeposited material was analyzed for many impurities; their concentrations are listed in Table 2. The concentrations of metallic impurities were estimated through emission spectrographic analysis. Sulfur and carbon were quantified using LECO analyzers. Nitrogen and oxygen were determined through the vacuum fusion technique.

The grain size of the as-deposited material was sufficiently small to require its characterization by transmission electron microscopy (TEM). Specimens were jet-polished in a 12:8:5 mixture of phosphoric acid, sulfuric acid and water. Less than 3 V was required for good results. By coating one surface of a specimen with lacquer, the specimen could be thinned toward that surface only. The material near the surface that had been adjacent to the anodized titanium cathode was examined in this manner. The microstructure was fine-grained; no grains exceeding 100 nm in diameter (Fig. 7). A 15 μm thick specimen jet-polished from both sides (so that the plane of observation was approximately 7 μm from the cathode surface) exhibited

Table 2.

Electrodeposited nickel impurity concentrations.

impurity	concentration (ppm)
C	< 50
S	< 20
O	70
N	20
Co	20
Cu	< 5
Fe	< 10
Mn	10
Pb	< 10
Si	< 5

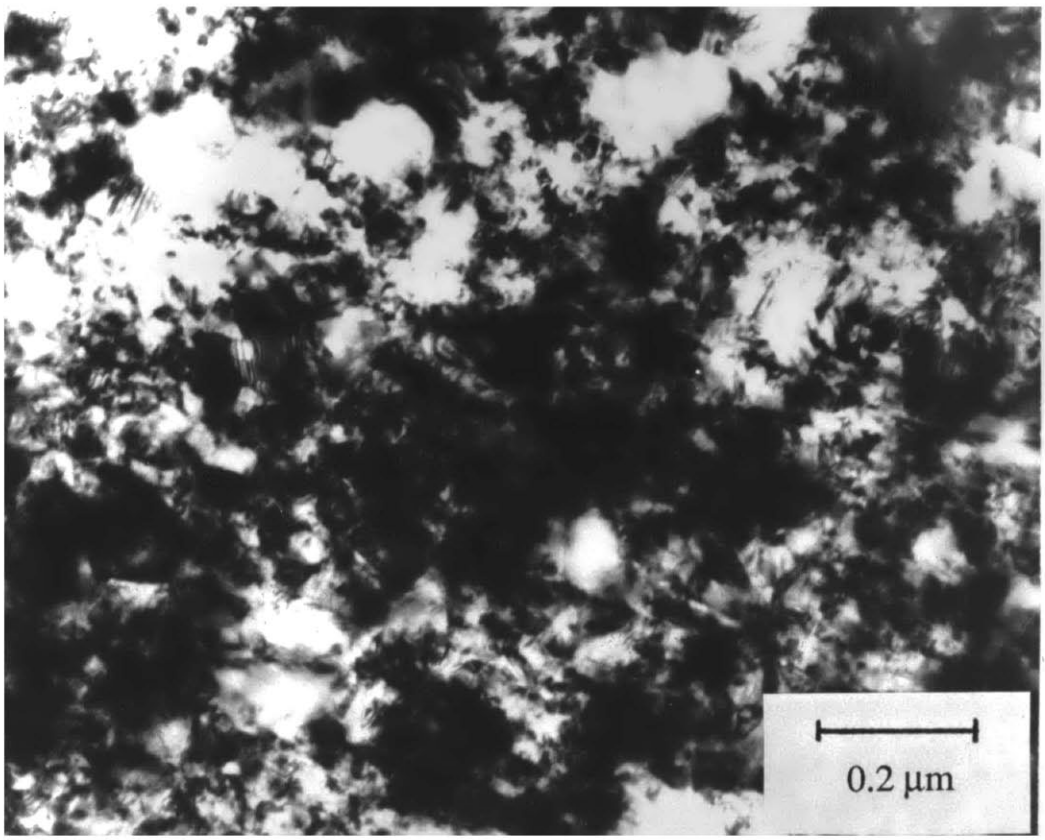

Fig. 7. Microstructure of electrodeposited nickel near surface that had been adjacent to the anodized titanium substrate. Only a few grains exceed 0.1 μm in diameter.

a microstructure typified by Fig. 8. Grains up to 0.5 μm were present, but fine-grained material predominated. The microstructure of a 50 μm thick specimen jet-polished from both surfaces is presented in Fig. 9. The larger grains were up to 2 μm in diameter. However, regions of fine-grained material persisted (Fig. 10). The microstructure of Figs. 9 and 10 was also typical of specimens more than 50 μm thick. The overall microstructure of an electrodeposited nickel foil is illustrated in Fig. 11.

Several heat treatments were employed to increase the grain size of the electrodeposited nickel; the conditions of each are listed in Table 3. Heat treatments denoted HT were conducted in a Pyrex tube purged continuously with argon. Following the desired time at temperature, the specimens were shifted to the unheated portion of the tube to enhance the rate of cooling. Specimens designated VA were vacuum-annealed and slowly cooled (the furnace was turned off, and the specimens were removed after it had returned to room temperature). In the SW treatment, the specimens were wrapped in stainless steel foil, and annealed in a standard furnace. This treatment included water quenching.

Materials HT-1 and HT-2 were jet-polished and characterized by TEM as described above. Typical microstructures are presented in Figs. 12 and 13. The most noticeable change brought about by these anneals was the progressive elimination of the fine-grained material. The larger grains in the HT-2 material were approximately 3 μm in diameter.

Metallographic characterization of the grain size was possible with the HT-3, VA and SW materials; representative micrographs are presented in Figs. 14-17. The HT-3 material was mounted in epoxy, mechanically ground and polished, and then chemically etched in a 1:1 mixture of nitric and acetic acids. The VA and SW specimens were first electropolished (using a 3:2 mixture of sulfuric acid and water, a platinum cathode and 4.5 V) and then

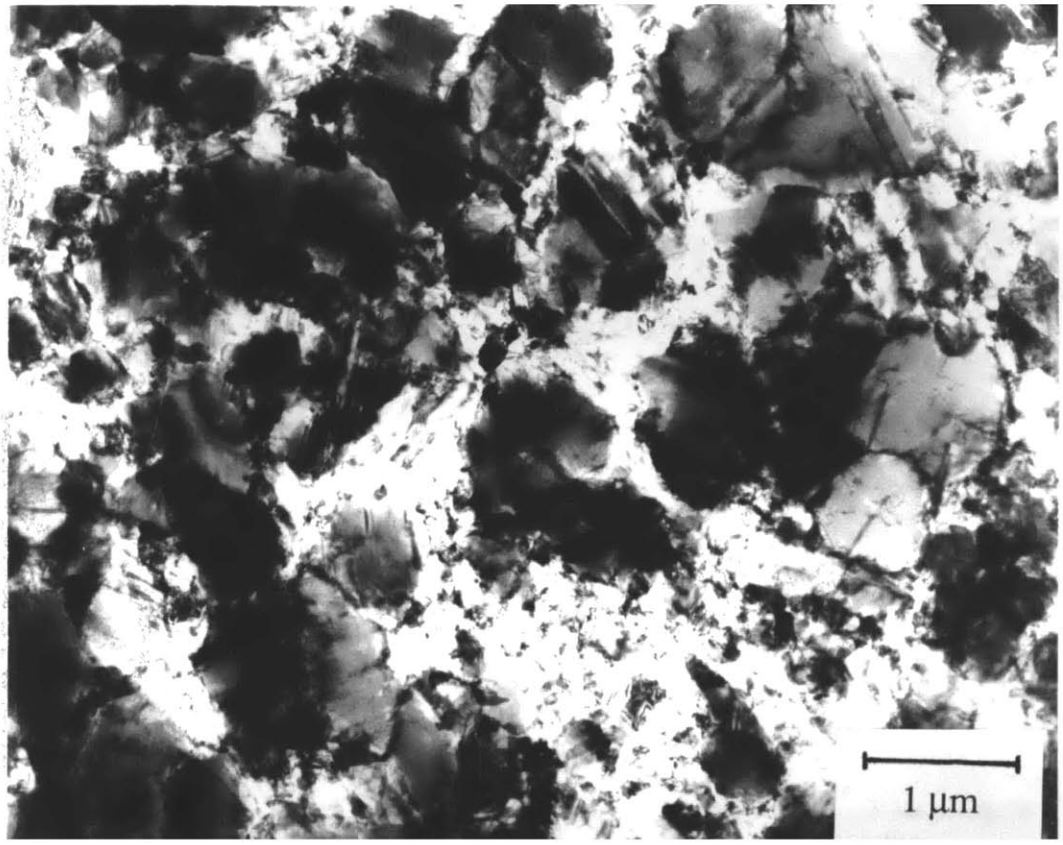

Fig. 8. Microstructure of electrodeposited nickel approximately 7 μm from surface that had been adjacent to the cathode surface. A few grains exceed 0.5 μm in diameter.

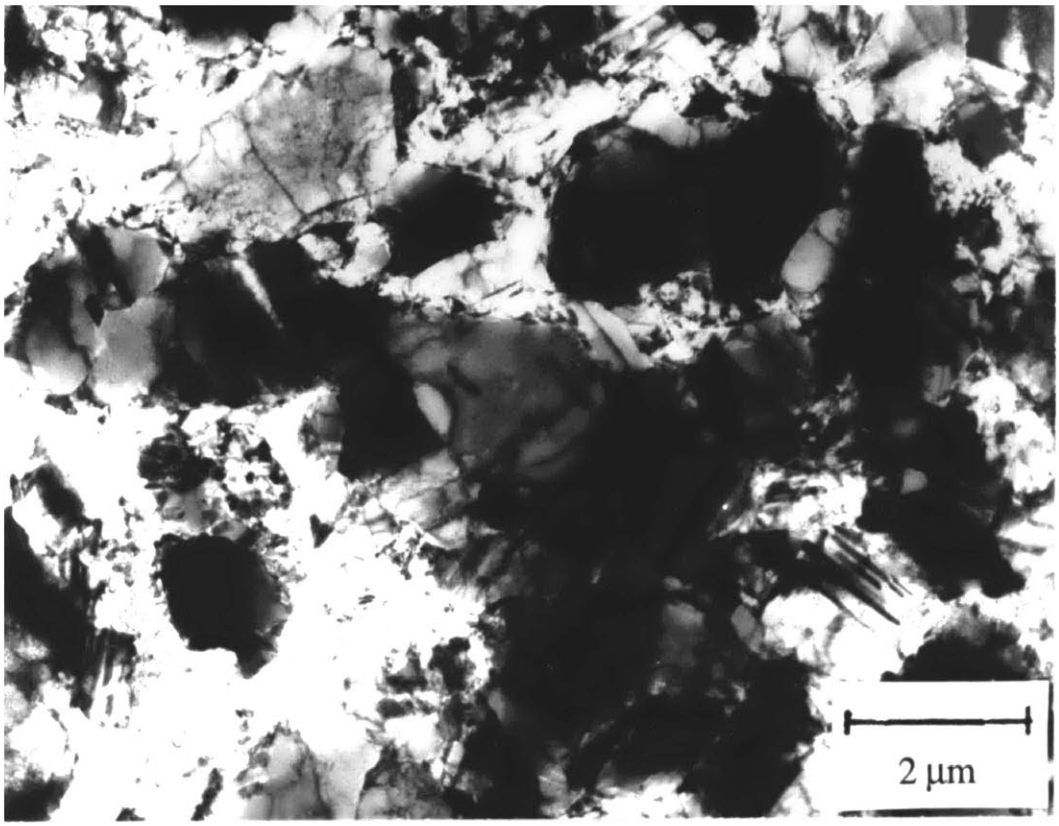

Fig. 9. Microstructure typical of electrodeposited nickel more than 25 μm from the surface that had been adjacent to the cathode. A few grains approach 2 μm in diameter.

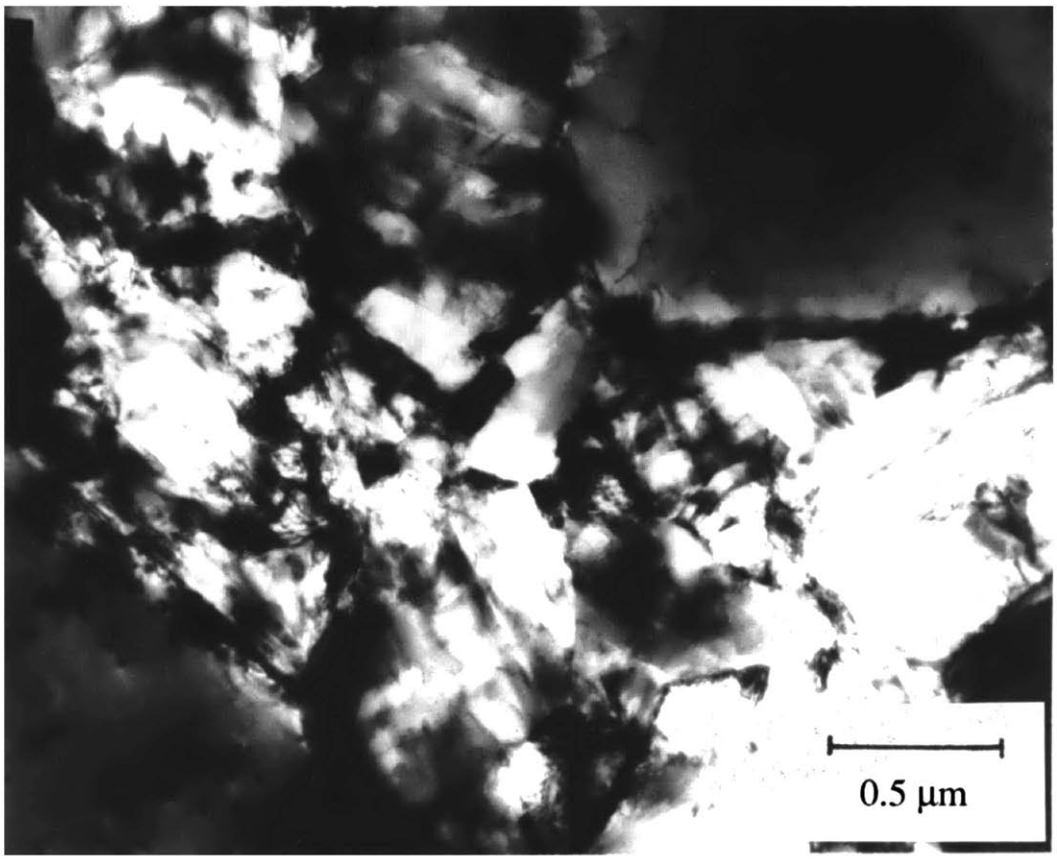

Fig. 10. Fine-grained material between larger grains in microstructure typical of electrodeposited nickel more than 25 μm from surface that had been adjacent to cathode.

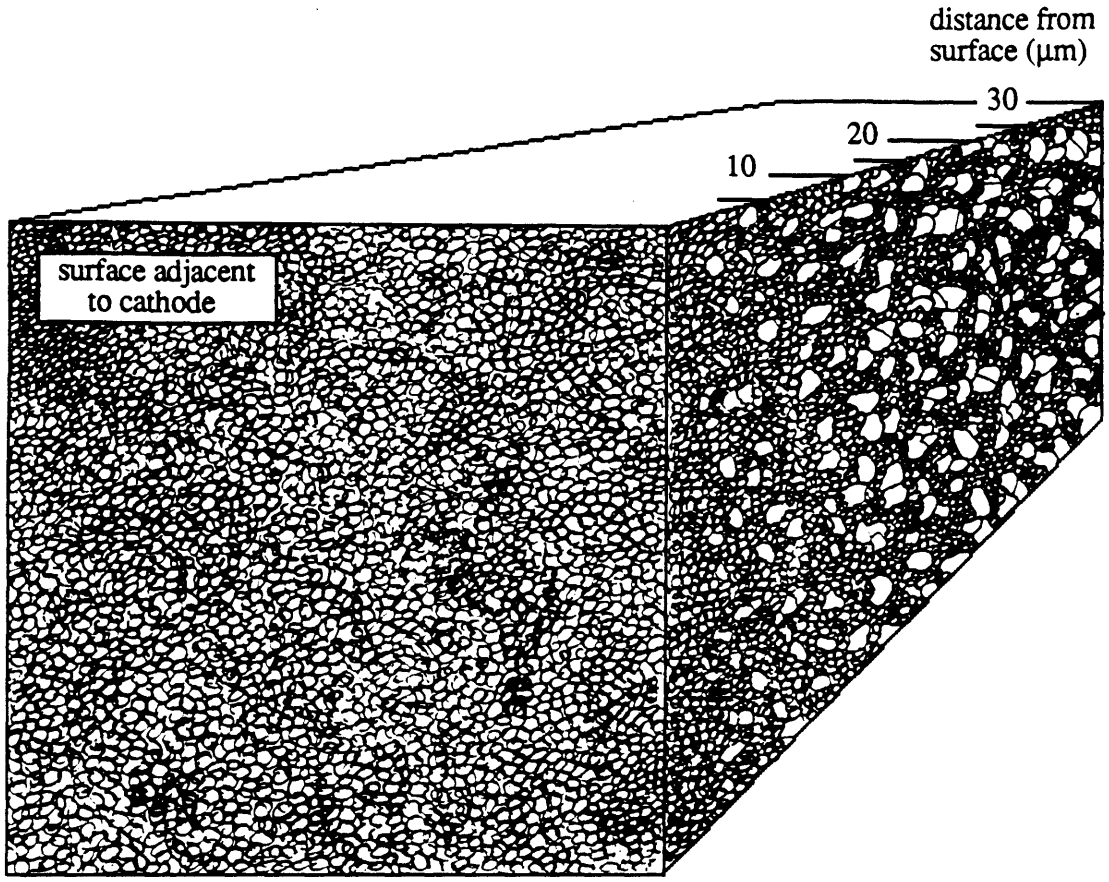

Fig. 11. Schematic illustration of the microstructure of electrodeposited nickel as a function of deposit thickness. Average grain size increases with increasing distance from the cathode, but regions of fine-grained material are present throughout specimen.

Table 3.

Heat treatment conditions.

	temperature	time	atmosphere	cooling
HT-1	300 °C	1 hr	flowing Ar	flowing Ar
HT-2	600 °C	30 min	flowing Ar	flowing Ar
HT-3	650 °C	1 hr	flowing Ar	flowing Ar
VA-1	800 °C	2 hr	vacuum	turned furnce off
VA-2	900 °C	3 hr	vacuum	turned furnace off
SW	1000 °C	10 min	air	water quench

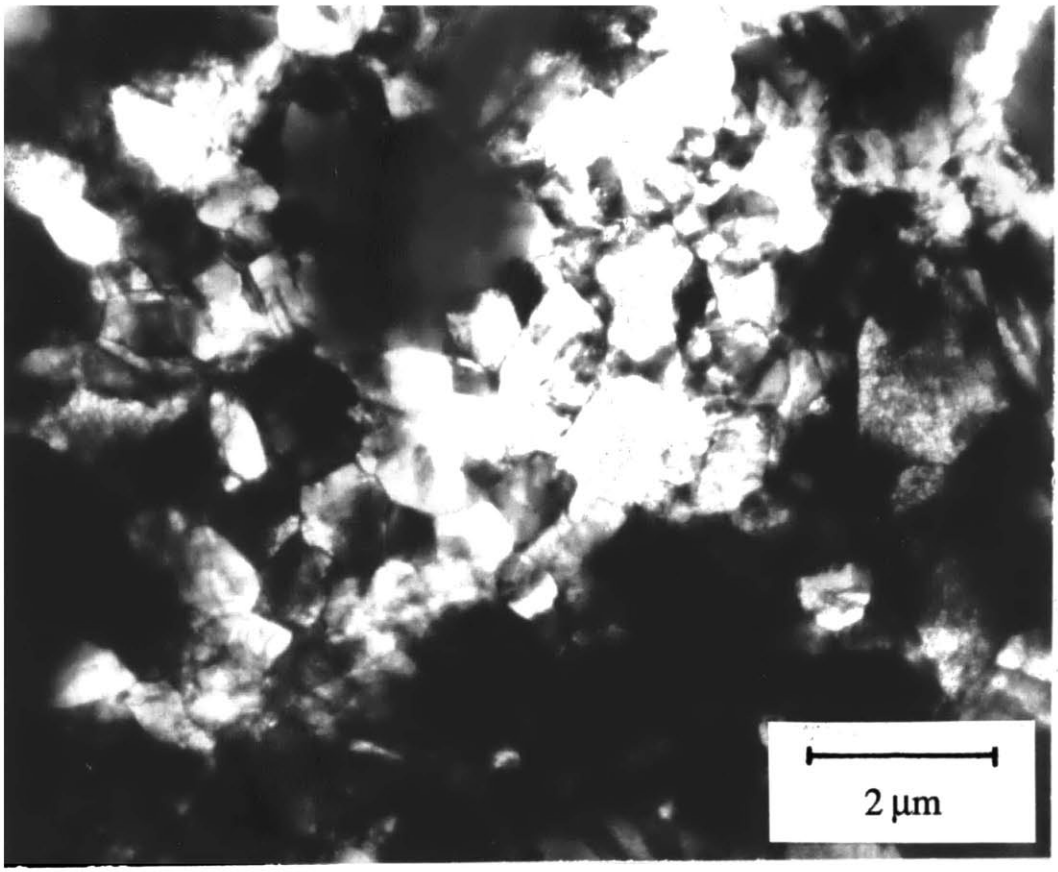

Fig. 12. Microstructure of HT-1 material (electrodeposited nickel, annealed for one hour at 300°C). Many of the smallest grains have been eliminated, but the large grains are still approximately 2 μm in diameter.

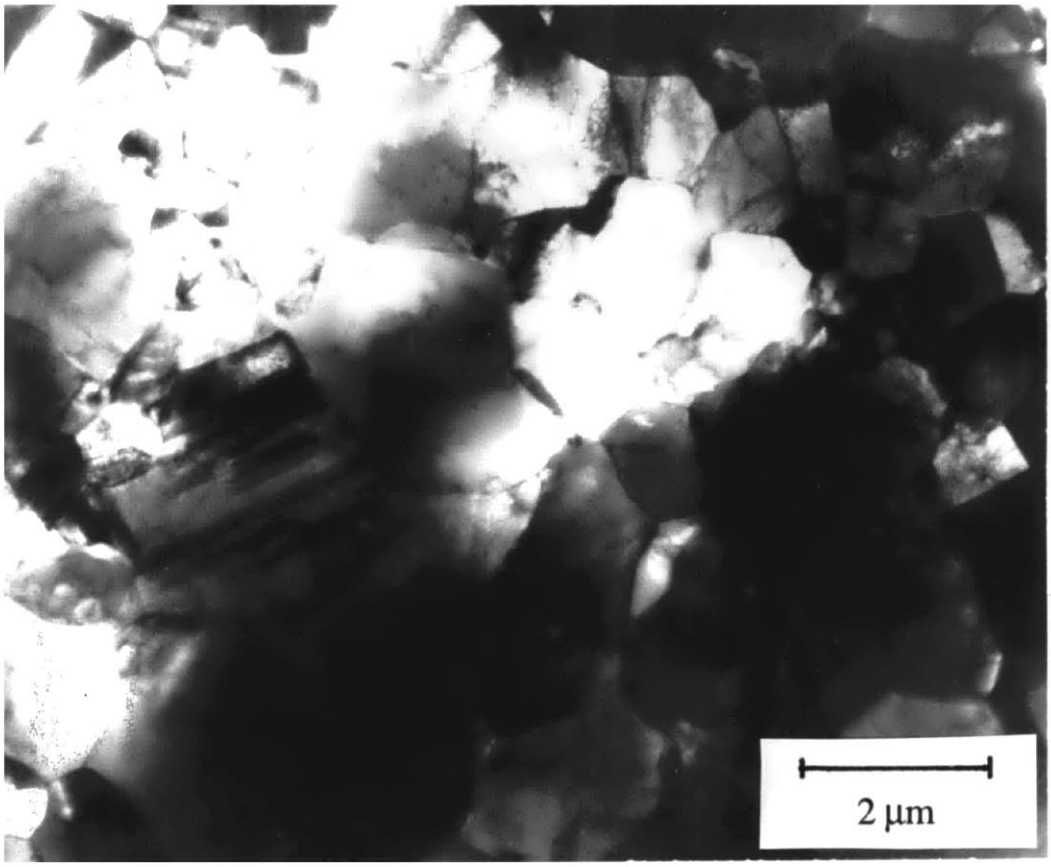

Fig. 13. Microstructure of HT-2 material (electrodeposited nickel, annealed for 30 minutes at 600°C). Few grains are less than 1 μm, or more than 3 μm, in diameter. The mean linear intercept is 1.3 μm.

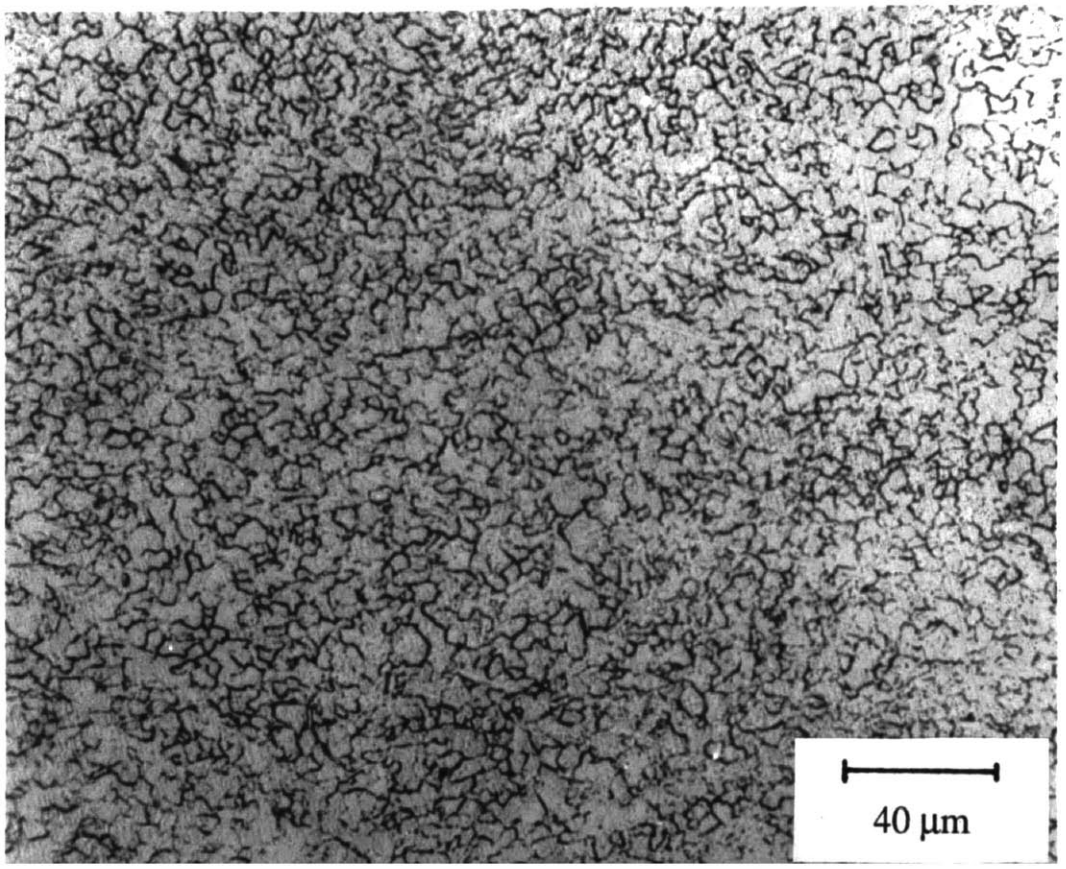

Fig. 14. Microstructure of HT-3 material (electrodeposited nickel, annealed for one hour at 650°C). The mean linear intercept is 4 μm.

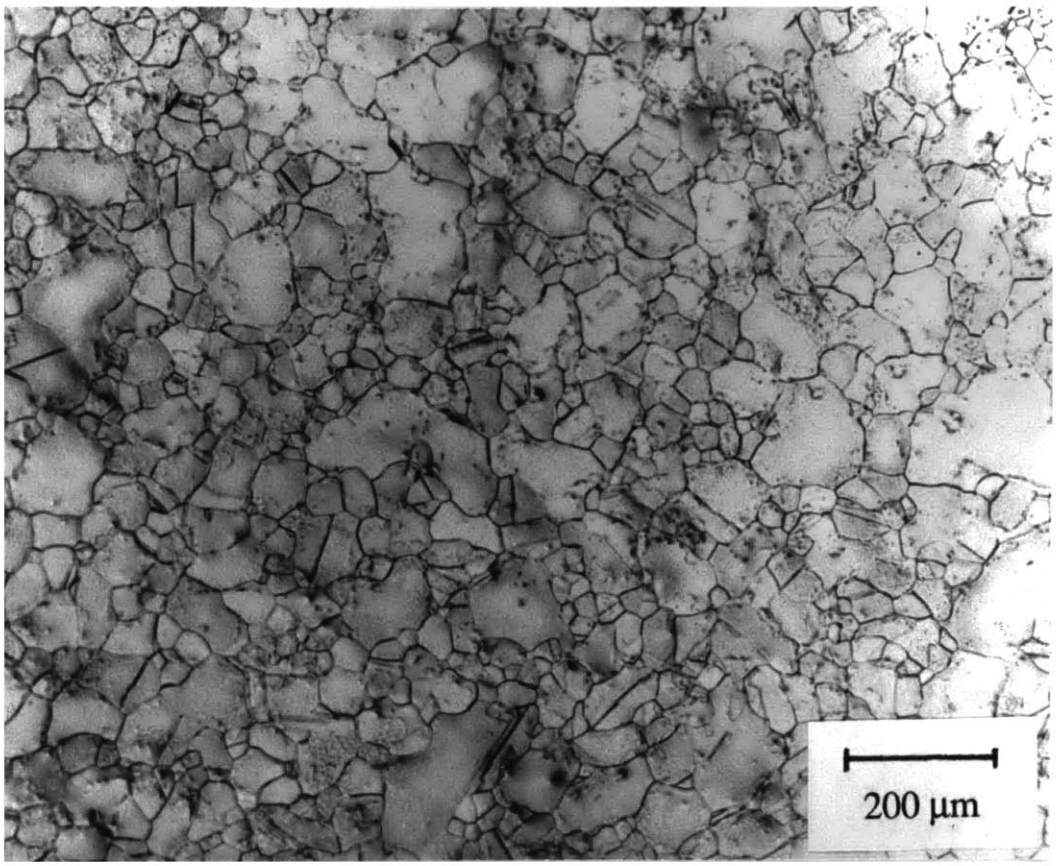

Fig. 15. Microstructure of VA-1 material (electrodeposited nickel, annealed for two hours at 800°C). The mean linear intercept is 20 μm. Pits that form around second phase particles during electropolishing are visible.

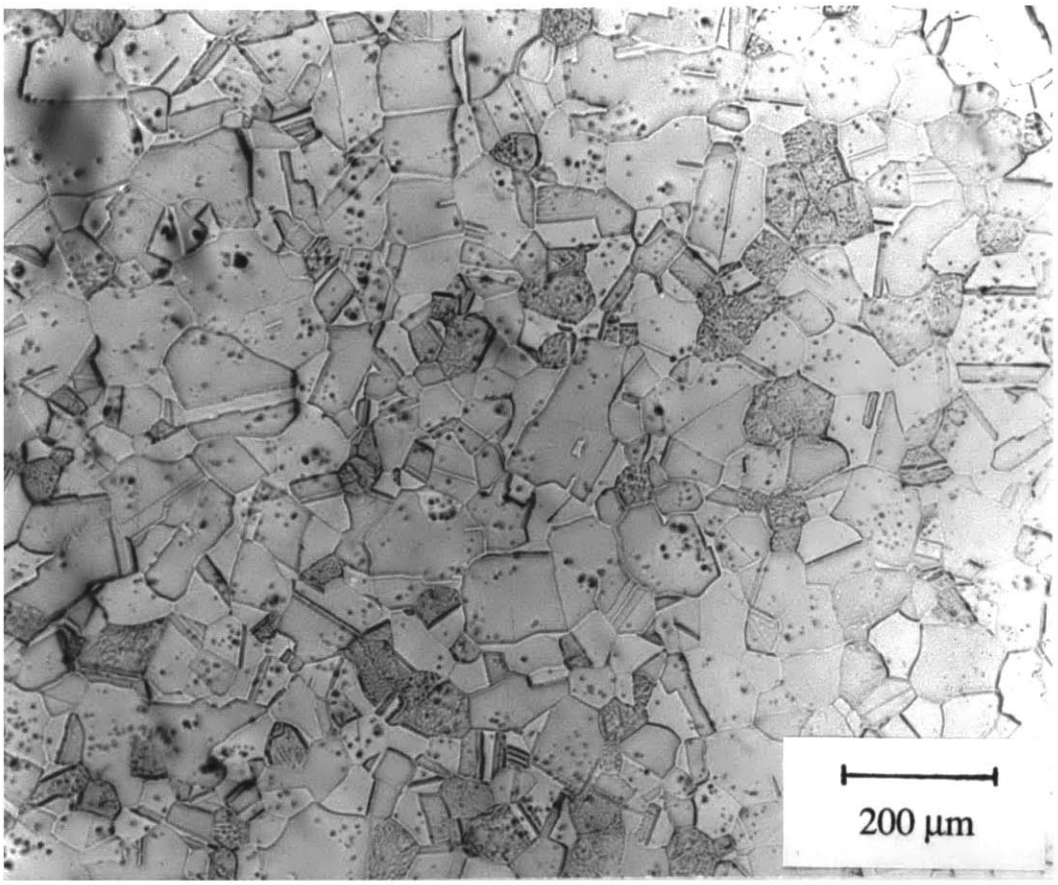

Fig. 16. Microstructure of VA-2 material (electrodeposited nickel, annealed for three hours at 900°C). The mean linear intercept is 44 µm. Pits due to second phase particles are now well-defined.

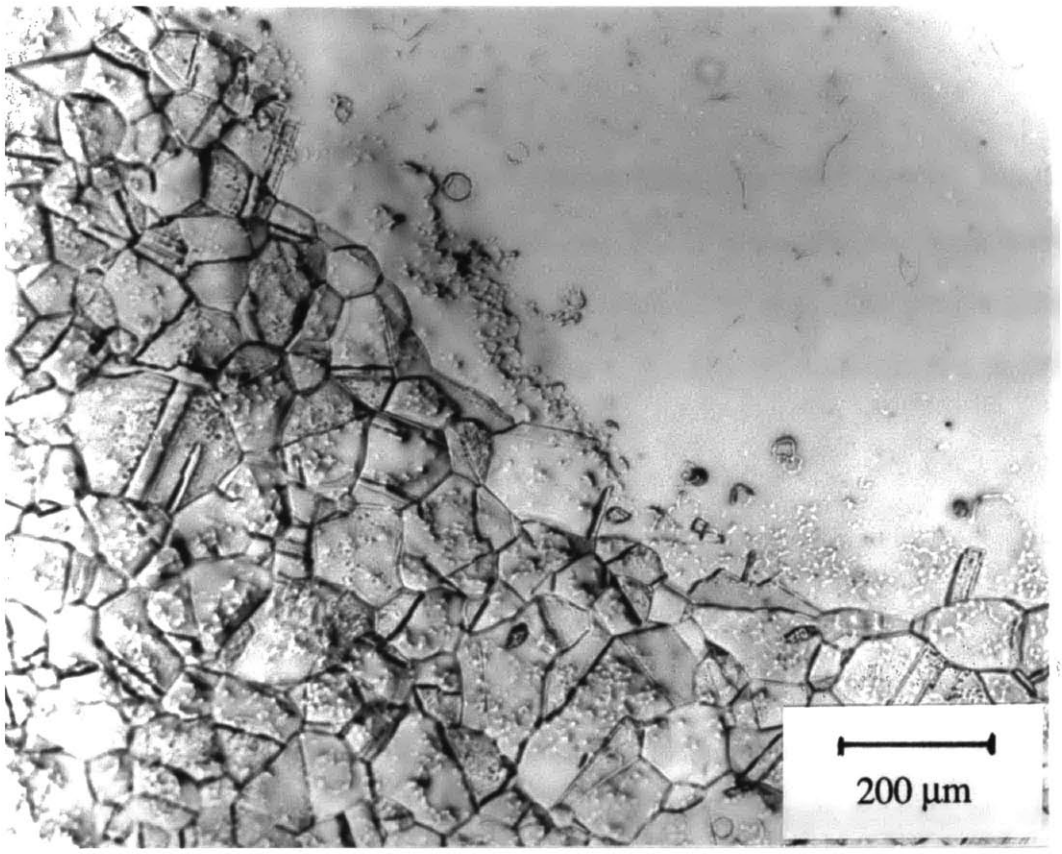

Fig. 17. Microstructure typical of SW material (electrodeposited nickel, annealed for ten minutes at 1000°C) is mixture of grains less than 200 µm, and greater than 1000 µm, in diameter.

electrolytically etched by simply reducing the voltage below the electropolishing regime. The electroetch was more difficult to control than the chemical etch, but provided a more uniform etch of the VA materials.

The grain size increased steadily through the HT-3, VA-1 and VA-2 anneals. The grain size distribution of each material was relatively narrow. Second phase particles were visible in the VA and SW materials. The SW heat treatment produced abnormal grain growth; grains up to 1.5 mm in diameter were visible, but the majority of grains were much smaller. Interestingly, only the abnormally large grains electropolished.

4.2. The Electrochemical Permeation Technique

Hydrogen is induced to permeate across a thin foil specimen by creating different concentrations on the two major surfaces. In the present study, the high and low concentrations were established electrochemically. A schematic diagram of the reaction pathways is presented in Fig. 18. Cathodic polarization of the "input" surface increases the concentration of adsorbed hydrogen, which in turn increases both the flux of hydrogen into the nickel and the evolution of hydrogen gas into the electrolyte. Unlike palladium, whose permeation behavior is described in the appendix, only a small fraction of the total hydrogen absorbs into nickel. The absorbed hydrogen diffuses to the "output" surface, where it is immediately oxidized in response to the anodic potential applied to this surface. Thus, a zero concentration boundary condition is created.

The permeation cell, illustrated in Fig. 19, consisted of two Pyrex glass chambers. The specimen was sandwiched between two O-ring fittings. Viton fluorocarbon polymer O-rings provided the seal. The O-ring fitting possessed some dead volume in which H_2 bubbles were intermittently trapped. This phenomenon resulted in significant variations in the effective area

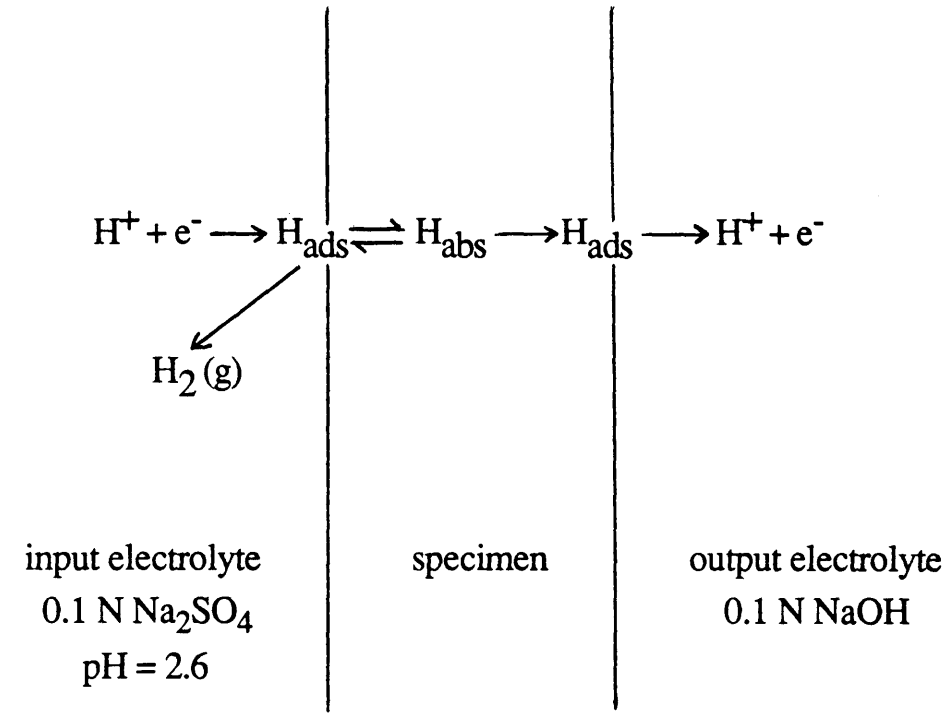

Fig. 18. Reactions involved in hydrogen permeation with electrochemical boundary conditions.

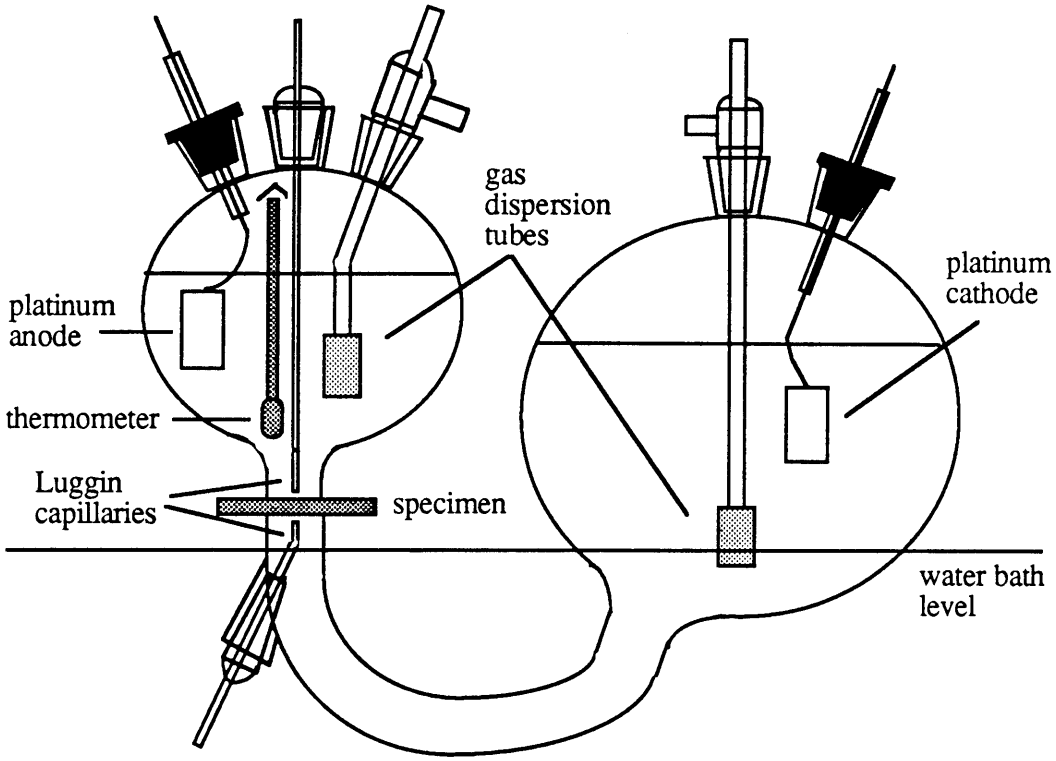

Fig. 19. Two-compartment electrochemical cell in which hydrogen permeation is measured.

of the input surface (i.e., the surface to which hydrogen is introduced), and consequently, the permeation current density measured at the output surface. To overcome this problem, the dead volume was eliminated by fitting another O-ring inside of the first (which seats in a groove). Concentric O-rings were also required on the output side to obtain a good seal. With this arrangement, the surface area exposed to electrolyte was 1.77 cm^2.

Each chamber was equipped with gas dispersion and exhaust tubes, allowing the electrolyte to be continuously bubbled with nitrogen gas to reduce the concentration of oxygen, and to provide mixing. Temperature control was complicated by the fact that the specimen could not contact water. Thus, only the lower portion of the output chamber (see Fig. 19) was submerged in a constant-temperature bath. Those portions of the cell above the water level were wrapped with a silicone rubber-coated heating tape (powered by a variable transformer) and enclosed in a cage of polystyrene foam. The temperature was monitored with a thermometer whose tip was approximately 2 cm from the input surface. This temperature and that of the constant-temperature bath were adjusted to within 1 °C of each other before starting an experiment.

The output surface was maintained at the desired anodic potential through the use an Aardvark model V-2LR potentiostat. This instrument satisfied the one critical requirement of electrochemical boundary conditions: the permeation specimen must be at floating ground with respect to both input and output electrical circuits (Fig. 20). The counter electrode was a platinum sheet with approximately 6 cm^2 of surface area. A saturated calomel electrode served as the reference. In order to minimize the error due to potential drop in the electrolyte, the reference electrode was connected to the electrolyte by a Luggin capillary whose fine tip was positioned approximately 1 mm from the nickel surface. A Pyrex glass stopcock and an agar bridge were included in this connection to reduce the transport of chloride ion to the alkaline

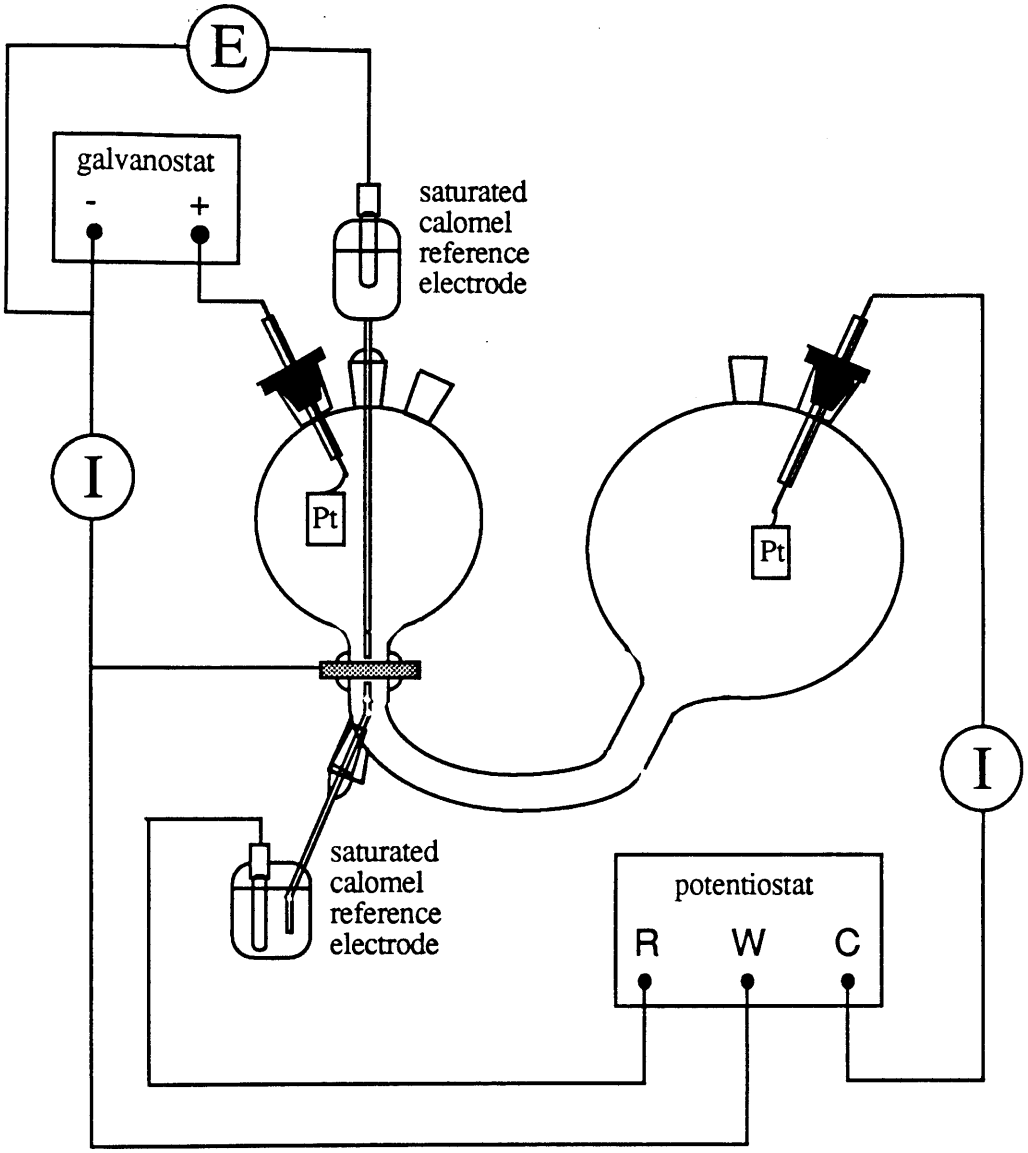

Fig. 20. Circuit diagram for hydrogen permeation with electrochemical boundary conditions.

electrolyte (this anion is known to break down passivity, which would result in an unacceptably high background signal). Tygon tubing and polyethylene quick-connections were also used in this isolation system. The oxidation current density, which is a measure of the flux of hydrogen through the specimen, was monitored with a Keithley model 602 electrometer and a standard strip chart recorder.

Anodic polarization of most metals will result in an increase in the rate of metal dissolution. However, nickel exhibits passivity over a well-defined range of anodic potentials. In alkaline electrolytes, the passive current density of nickel is particularly small. Thus, the output surface was polarized to 0.10 V_{SCE} in 0.1 N NaOH, which resulted in a background current density less than 0.2 $\mu A/cm^2$ after several hours of polarization.

To produce hydrogen permeation, a constant cathodic current was applied to the input surface. Another Aardvark model V-2LR served as the galvanostat. The counter electrode was a platinum sheet with approximately 6 cm^2 of surface area. The input electrolyte was 0.15 N Na_2SO_4, acidified with sulfuric acid to pH 2.6. Analytical-grade reagents and distilled water (18 $M\Omega$/cm conductivity) were used in its preparation. This electrolyte has been shown to allow the oxide film formed on nickel during electropolishing (or simple exposure to air) to be quickly reduced under moderate cathodic polarization (36). The potential of the input surface was monitored with reference to another saturated calomel electrode. A chloride ion isolation system similar to that described above was also used in this case.

The maximum cathodic current density routinely used in this study was 34 mA/cm^2. Even with this relatively-low value, a slow but steady increase in the temperature of the input electrolyte was detected. This behavior is due to Joule heating (22). The cell design featuring the horizontally oriented specimen (Fig. 19) was chosen to minimize this problem.

The as-deposited foils were oriented so that the surface that had been adjacent to the anodized titanium substrate served as the output surface. The smoothness of this surface (due to the smooth surface of the anodized titanium cathode), provided a lower passive current density than the matte finish exhibited by the other surface. The matte finish also proved to be a better input surface (see section 6.2).

The heat treatments given to the electrodeposited specimens resulted in smoother input surfaces which were more susceptible to contamination from the electrolyte (see section 6.2). This problem was partially overcome by etching the input surface with a 1:1 mixture of acetic and nitric acids for 10 seconds (followed by thorough rinsing with distilled water). The effect of this treatment was not permanent, but it could be repeated without removing the specimen from the permeation cell, or even interrupting anodic polarization of the output surface.

5.0. Results

As noted in the previous section, the boundary conditions for permeation were produced electrochemically. The initial condition was produced in the same manner. Prior to the first experiment, the output surface was anodically polarized for several hours so that the current corresponding to nickel dissolution could decay to a very small value. This treatment also served to remove atomic hydrogen dissolved in the nickel during its electrodeposition. Thus, the initial condition for the first permeation experiment approximated that of zero hydrogen throughout the specimen.

The permeation experiment begins with the application of a constant cathodic current to the input surface. An example of the transient in the oxidation current density measured on the output surface (referred to below as the permeation current density) is presented in Fig. 21. After a short period of time, hydrogen "breaks through" the specimen and the permeation current density increases. At long times, the permeation current density attains a steady state value. This behavior corresponds to the development of a steady state concentration gradient across the foil specimen (Fig. 22). The concentration of absorbed hydrogen just beneath the input surface is referred to below as the input concentration (C_o). Ideally, this quantity is constant throughout the experiment (i.e., a constant concentration input boundary condition is produced by the constant cathodic current applied to the input surface).

It is desirable to perform more than one permeation experiment on each specimen. Unfortunately, it is difficult to reestablish the zero concentration initial condition when the input surface concentration is controlled electrochemically. Application of an anodic potential to the input surface will result in the oxidation of nickel as well as hydrogen. The amount of nickel consumed can be minimized by applying a potential corresponding to the passive

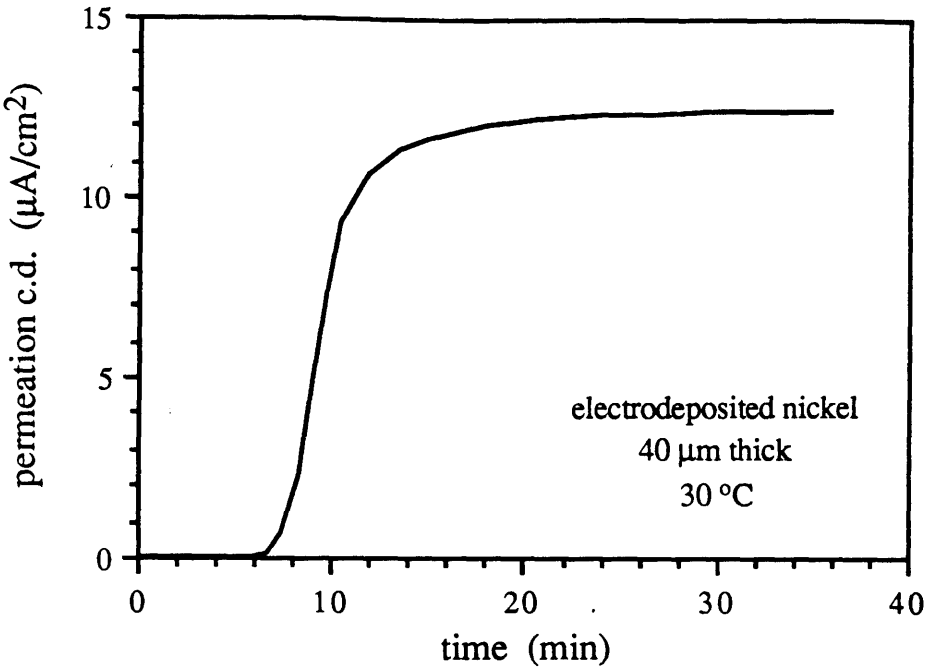

Fig. 21. Transient in the permeation current density (measured on the output surface) resulting from the application of a cathodic current to the input surface.

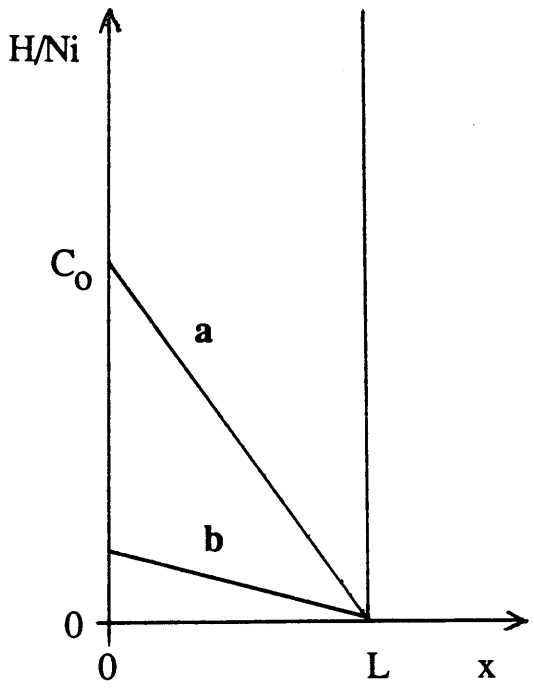

Fig. 22. Concentration profiles in the thin foil specimen corresponding to: **a**) steady state permeation and **b**) cathodically protected input surface (initial condition).

domain. However, the passive film on the surface may adversely affect the absorption of hydrogen in subsequent tests. Nickel dissolution can be eliminated by applying a small cathodic current density to the input surface. The initial condition corresponding to a cathodically protected input surface is a steady-state hydrogen concentration gradient (Fig. 22).

With electrodeposited nickel specimens, the two initial conditions described above result in radically different permeation transients (Fig. 23). Transient **a** corresponds to the zero hydrogen initial condition and a cathodic current density (i_c) of 17 mA/cm^2 applied to the input surface to produce permeation. Transient **b** was produced by the same value of i_c, but the initial condition was the steady state concentration gradient corresponding to an initial cathodic current density of 0.17 mA/cm^2. Thus, with some hydrogen present in the specimen initially, less time is required to attain steady state permeation.

The diffusion coefficient can be determined from permeation data in two different ways. The most commonly-used method is based on a comparison of the experimental transient and theoretical transients obtained by solving Fick's Second Law (with the initial and boundary conditions described above and various values of the diffusion coefficient). This process can be made more expeditious by employing one of several parameters related to characteristic features of the transient. The parameter used in the present study is known as the lag time (t_L). It is defined by the expression (37):

$$i\,(t_L) - i_o = 0.63\,(i_{ss} - i_o) \qquad [2]$$

where i_o = current density at the output surface at the beginning of the permeation experiment

i_{ss} = steady-state permeation current density.

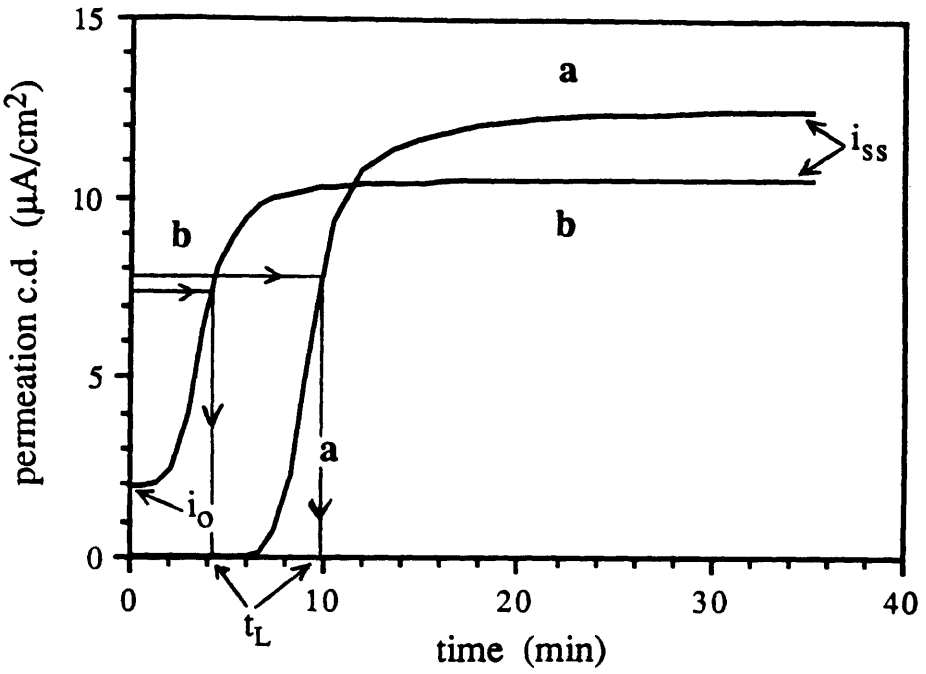

Fig. 23. Effect of the initial condition on the transient in the permeation current density produced by a cathodic current density of 17 mA/cm^2 applied to the input surface. Transient **a** resulted from a zero concentration initial condition; transient **b** resulted from an initial steady state concentration gradient (produced with a cathodic current density of 0.17 mA/cm^2). Determination of the lag time (with equation [2]) is illustrated for both transients.

The initial current density associated with the first permeation experiment is due solely to the oxidation of nickel. In subsequent experiments, hydrogen permeation resulting from the steady state concentration gradient initial condition will also contribute to i_o. Determination of the lag time is illustrated for both permeation transients in Fig. 23.

The relationship between D and t_L was derived by Barrer (38):

$$D = \frac{L^2}{6\, t_L} \qquad [3]$$

where L = specimen thickness.

As the two transients in Fig. 23 are produced with the same specimen, it would appear that the lag time can have more than one value. This illustrates the drawback associated with determination of the diffusion coefficient from the permeation transient: this value is reduced by trapping of hydrogen at crystalline defects. Increasing the initial hydrogen content saturates a portion of the trap sites, resulting in a decrease in the lag time and a corresponding increase in D. Due to the possible influence of trapping, the diffusion coefficient determined from the permeation transient is usually referred to as the "effective" or "apparent" diffusion coefficient (D_{eff}). The value of D_{eff} corresponding to transient **b** in Fig. 17 is 1.3×10^{-12} m^2/s.

The diffusion coefficient can also be determined from the steady state permeation current density. This parameter is not affected by trapping (for an explanation of the difference in the steady state permeation current density between the two transients in Fig. 23, see section 6.2). Therefore, the diffusion coefficient determined from it, referred to below as the true diffusion

coefficient, is also free of this complication. The steady-state permeation current density is related to the true diffusion coefficient (D) by Fick's First Law:

$$i_{ss} = \frac{F D C_o}{L} \qquad [4]$$

where F = the Faraday
C_o = input concentration.

The input concentration is required in this calculation. Unfortunately, a meaningful value of this parameter cannot be determined in a material containing numerous trap sites such as the electrodeposited nickel. However, C_o could be estimated from the permeation behavior of the material produced by the VA-2 heat treatment. The effective diffusion coefficient for hydrogen in these specimens at 30°C was determined to be 7.8×10^{-14} m^2/s. This value is in agreement with the "best" value determined by Robertson (20) in his review of studies of hydrogen diffusion in nickel conducted prior to 1973. This "best" value is an extrapolation from permeation measurements conducted at high temperatures, where the effect of trapping on hydrogen diffusion is greatly diminished. Thus, trapping does not affect hydrogen diffusion in the VA-2 material, and the value of D_{eff} noted above can be used in equation [4] to calculate C_o. The input concentration varied with the cathodic current density applied to the input surface (i_c) according to Fig. 24.

Assuming that the relationship between C_o and i_c in Fig. 24 holds for the electrodeposited nickel as well as the VA-2 material, equation [4] can be solved for the true diffusion coefficient of the former. Values of D determined for several specimens averaged 3.3×10^{-12} m^2/s, which is more than two times larger than the D_{eff} value corresponding to transient **b** in Fig. 23. Thus, it is clear that the initial condition produced by a cathodic current density of 0.17 mA/cm^2 does not saturate all the hydrogen trap sites. The average value of D is more

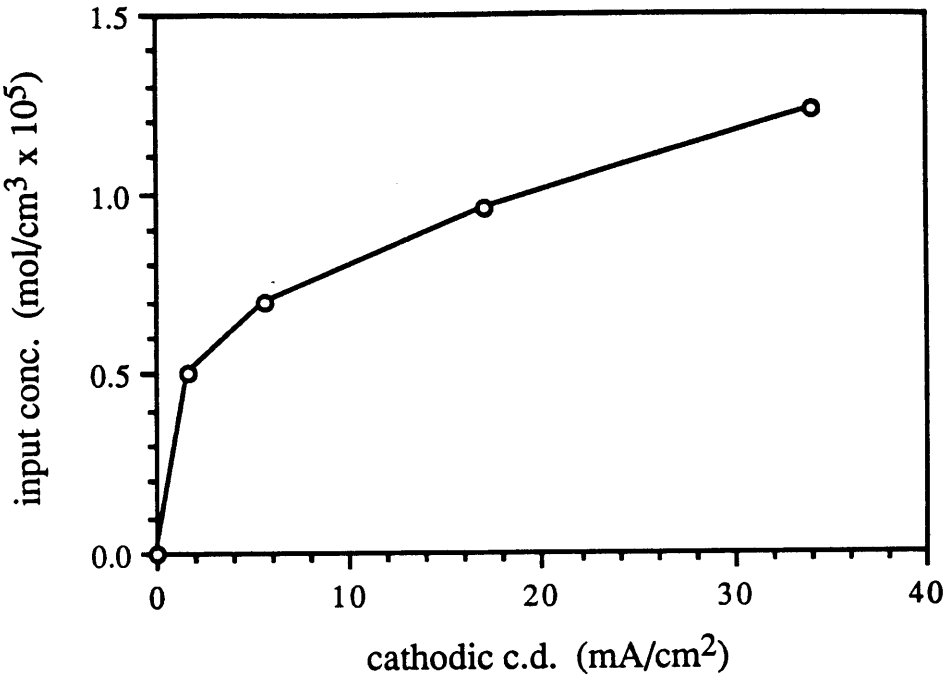

Fig. 24. Relationship between the cathodic current density and the input hydrogen concentration at 30 °C determined with VA-2 specimens.

than forty times larger than the diffusion coefficient determined for the VA-2 material.

All of the permeation experiments described above were conducted at 30 °C. A knowledge of the effect of temperature on the diffusion of hydrogen in the electrodeposited nickel was also desired. Both D_{eff} and D were determined over the temperature range 22-72 °C. In the latter case, the temperature dependence of the input concentration was needed. This relationship was also determined with VA-2 specimens. The temperature dependence of the diffusion coefficient for this material was:

$$D_{eff} = 0.012 \exp\left(\frac{-41000}{RT}\right) \qquad [5]$$

where R = gas constant
T = absolute temperature.

This expression is in agreement with the "best" expression determined by Robertson (20). The correspondence confirms that trapping is negligible in the VA-2 material. Therefore, the D_{eff} values could be used in equation [4] to calculate C_o values. These data are presented in the form of an Arrhenius plot in Fig. 25. A cathodic current density of 17 mA/cm^2 was used throughout this set of experiments.

Assuming that the relationship in Fig. 25 is valid for the electrodeposited nickel as well as the VA-2 material, the effect of temperature on the true diffusion coefficient for the former could be determined. Values of D determined with several specimens are presented in the form of an Arrhenius plot in Fig. 26. For comparison, the D_{eff} values determined from the same set of data (i_c = 17 mA/cm^2) are included in this figure. The activation energies calculated from the slopes are 14 kJ/mol for the true diffusion coefficient and 19 kJ/mol for the effective diffusion coefficient.

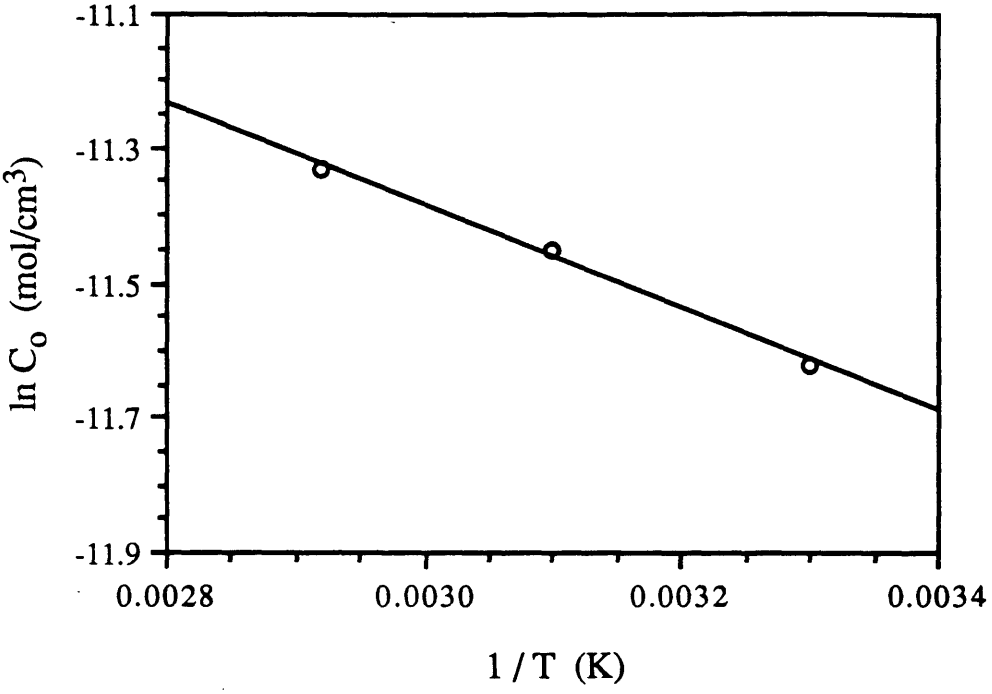

Fig. 25. Temperature dependence of the input hydrogen concentration produced with a cathodic current density of 17 mA/cm^2. This relationship was also determined with VA-2 specimens.

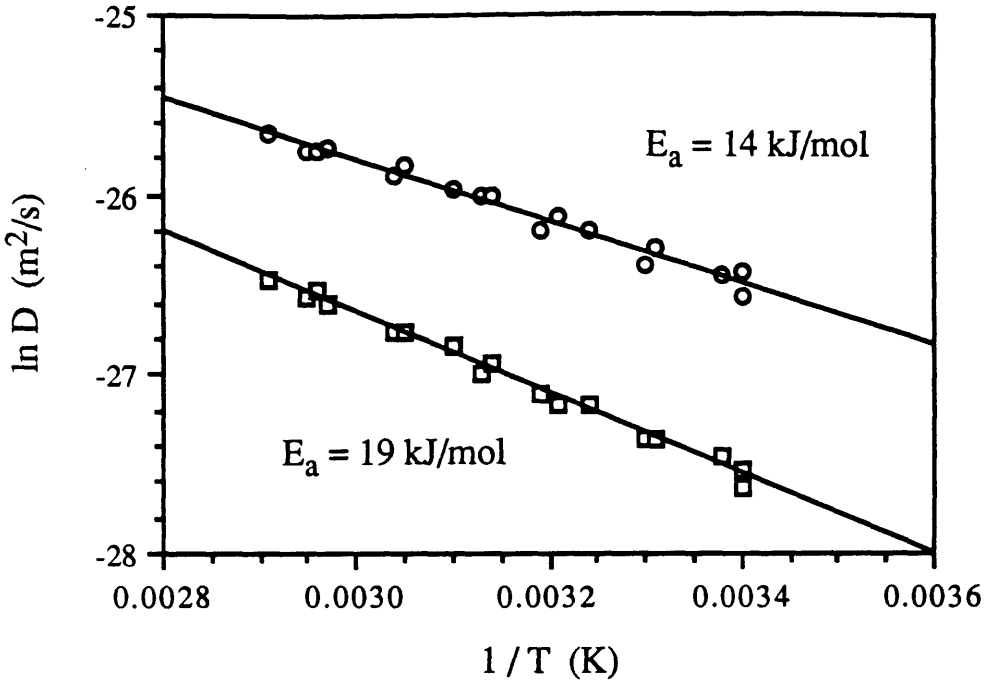

Fig. 26. Temperature dependence of the true (circles) and effective (squares) diffusion coefficients for hydrogen in electrodeposited nickel.

The permeation behavior of each set of heat-treated specimens was analyzed in a manner similar to that described above. The average grain diameter (39), the true diffusion coefficient at 30 °C, and the activation energy determined from an Arrhenius plot of true diffusion coefficients are listed for each material in Table 4.

Table 4.

Characteristics of electrodeposited and annealed nickel.

material	average grain diameter* (μm)	diffusion coefficient at 30°C (m^2/s)	activation energy (kJ/mol)
electrodeposited	†	3.3×10^{-12}	14
HT-1	†	1.4×10^{-12}	14
HT-2	1.3	8.8×10^{-13}	25
HT-3	4	1.3×10^{-13}	40
VA-1	20	7.7×10^{-14}	41
VA-2	44	7.8×10^{-14}	41

* Actually, the mean linear intercept, which is equivalent to the average grain diameter, was determined.

† The wide grain size distribution of this material did not allow a valid measurement of the mean linear intercept.

6.0. Discussion

6.1. Electrodeposited Specimens

Commercially-produced electrodeposits frequently exhibit "pores" that limit the ability of the coating to isolate the substrate from corrosive environments. Thus, there was concern that permeation specimens produced by electrodeposition might contain pinholes. The presence of a through-thickness pinhole was readily apparent in the permeation experiment: the permeation current density increased immediately upon the application of a cathodic current to the input surface. With the first few specimens produced in this study, it was noted that the percentage of specimens exhibiting pinholes decreased as the thickness of the specimen increased. This suggests that the pinholes close off as additional material is deposited. Closed-off pinholes represent thin spots in the specimen which can provide an artificially high permeation current, or even a two-stage transient. An example of the latter is presented in Fig. 27; the first rise and plateau in the permeation current density result from hydrogen permeation through one or more extremely thin regions of the specimen.

To address the issue of closed-off pinholes, several sets of specimens 15 μm in thickness were produced and permeation-tested. It was noted that for each set of specimens, the first one produced on the anodized titanium cathode usually contained through-thickness pinholes. When the cathode was immediately returned to the bath after the removal of the first specimen, the second specimen did not exhibit pinholes of either type. When three or four specimens were produced in this manner, all but the first were free of pinholes. Thus, it can be concluded that specimens produced on a clean substrate will not contain closed-off pinholes extending more than 15 μm into a deposit.

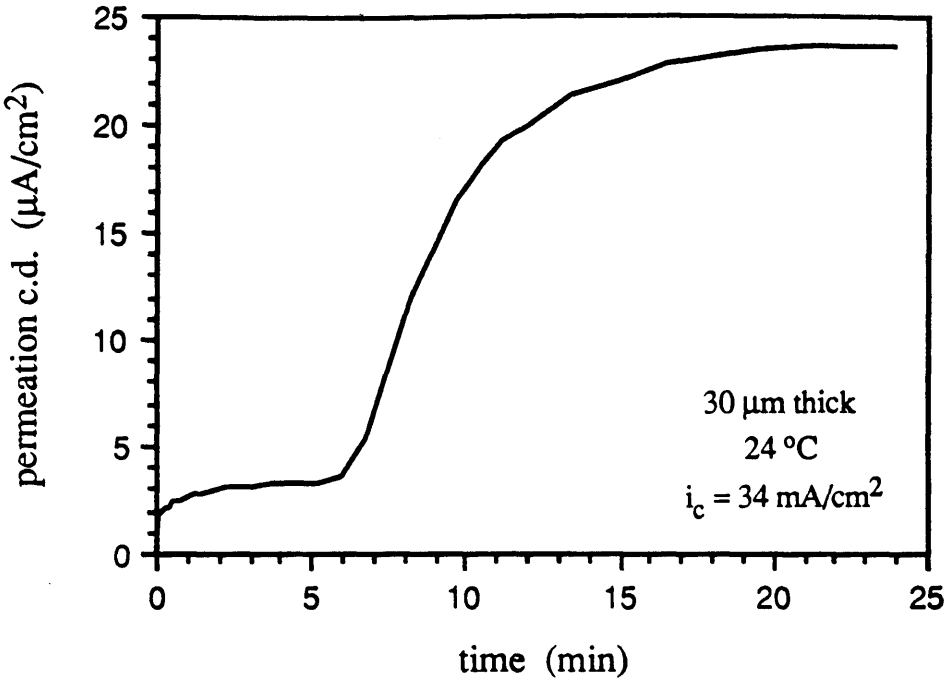

Fig. 27. Two-stage transient in the permeation current density resulting from the presence of one or more closed-off pinholes in the electrodeposited nickel specimen.

The observations above suggest that contamination of the cathode surface by some component of laboratory air was responsible for the nucleation of pinholes. As noted in section 4.1, the material near the surface that was adjacent to the cathode during electrodeposition could be examined by TEM. Large second-phase particles (Fig. 28) were discovered in the first specimen of each set above. No particles were observed in subsequent specimens. Thus, it appears that atmospheric particulates nucleate pinholes. This contamination is trapped in the first specimen, so that removal of the latter provides a clean surface for subsequent deposition.

As the test material was electrodeposited from a bath prepared with distilled water and analytical-grade chemicals, it was expected to be of high purity. The low concentrations of sulfur and carbon would suggest that little, if any, of the wetting agent is incorporated into the deposit. The most plentiful impurity was oxygen, presumably resulting from the incorporation of nickel hydroxide into the deposit (40). An high oxygen content is also characteristic of nickel electrodeposited from the Watt's bath, an electrolyte based on the sulfate and chloride salts of nickel (41).

Second phase particles were not observed by TEM in either the as-deposited or HT materials. However, the VA and SW anneals, which involved higher temperatures, promoted the precipitation of supersaturated solutes or allowed pre-existing inclusions to coarsen. The presence of second phase particles is clearly indicated by pits that develop during electropolishing (Figs. 15-17).

The second phase particles are responsible for the abnormal grain growth (also referred to as secondary recrystallization) observed with the SW heat treatment (Fig. 17). This phenomenon results from the localized breakdown of grain boundary pinning by the particles as their radii exceed a critical value through coarsening. Apparently, the rate of diffusion of the solute (s)

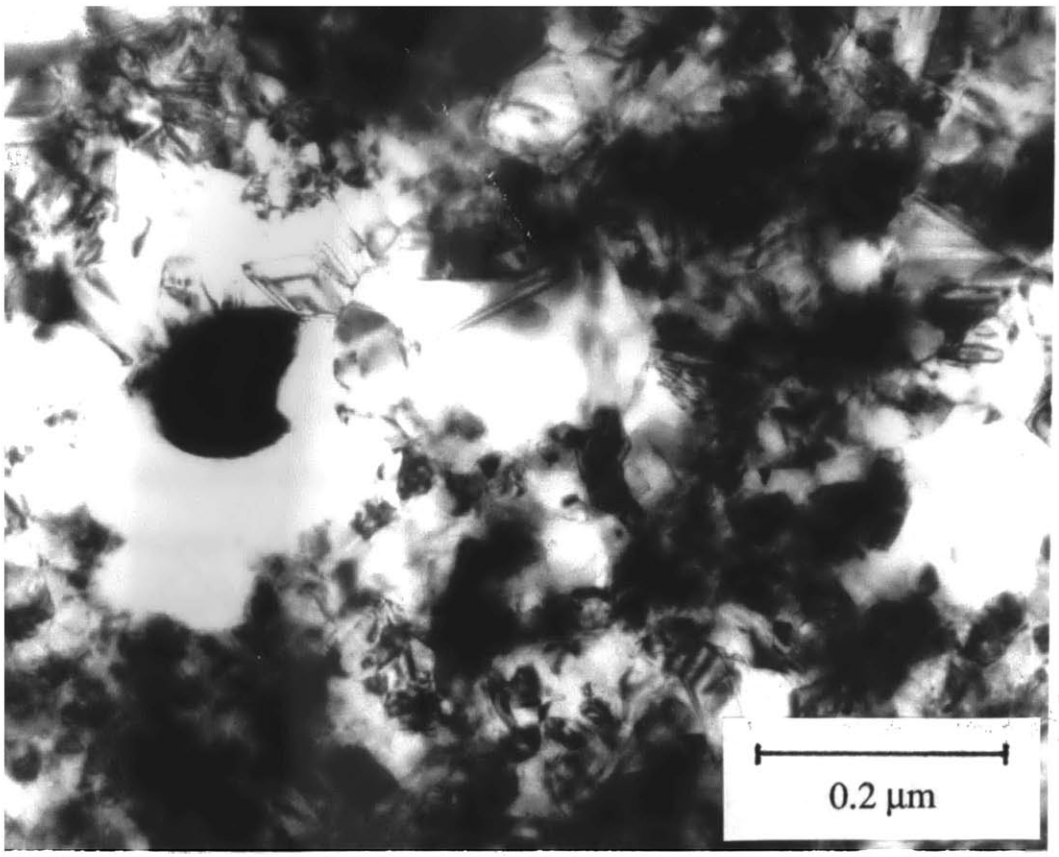

Fig. 28. Atmospheric particulate trapped in nickel electrodeposit (near the surface that had been adjacent to the anodized titanium cathode).

present in the second phase increases significantly when the temperature of the anneal is increased from 900 °C (the temperature of heat treatment VA-2) to 1000 °C (that of treatment SW), as abnormal grain growth is evident after only 10 min. at the higher temperature. In some cases, the second-phase particles appeared to be dragged by the most mobile boundaries (Fig. 29).

Thompson and Saxton (33) have reported that nickel electrodeposited from a sulfamate bath onto stainless steel (another nonbonding cathode material) exhibits a narrow grain size distribution, with an average grain diameter of 0.12 μm. Despite similar bath composition and operating conditions, the microstructure of the material produced in the present study was significantly different. The grain size of the material near the cathode surface was extremely small (Fig. 7), apparently due to poor lattice matching between nickel and the titanium dioxide coating. With increasing thickness, grains up to 2 μm in diameter were observed (Fig. 9). However, fine-grained material persisted as regions in between larger grains (Fig. 10).

An attempt was made to understand the factor(s) responsible for the different microstructures obtained in the two studies. The most obvious difference was the cathode. However, the stainless steel surface used by Thompson and Saxton must surely have been covered with an oxide film; otherwise, the specimens would have chemically bonded to the surface. Thus, its grain-refining effect on the microstructure of the electrodeposit would diminish in a manner similar to that observed with the anodized titanium cathode (Fig. 11).

Suoninen and Hakkarainen (42) have shown that the grain size of nickel electrodeposited from the Watt's bath decreases as the pH increases. They attributed this behavior to the formation of a nickel hydroxide film on the surface of the deposit that inhibits the growth of large grains. Since the pH of the bath used in the present study increased slightly with use, it is conceivable

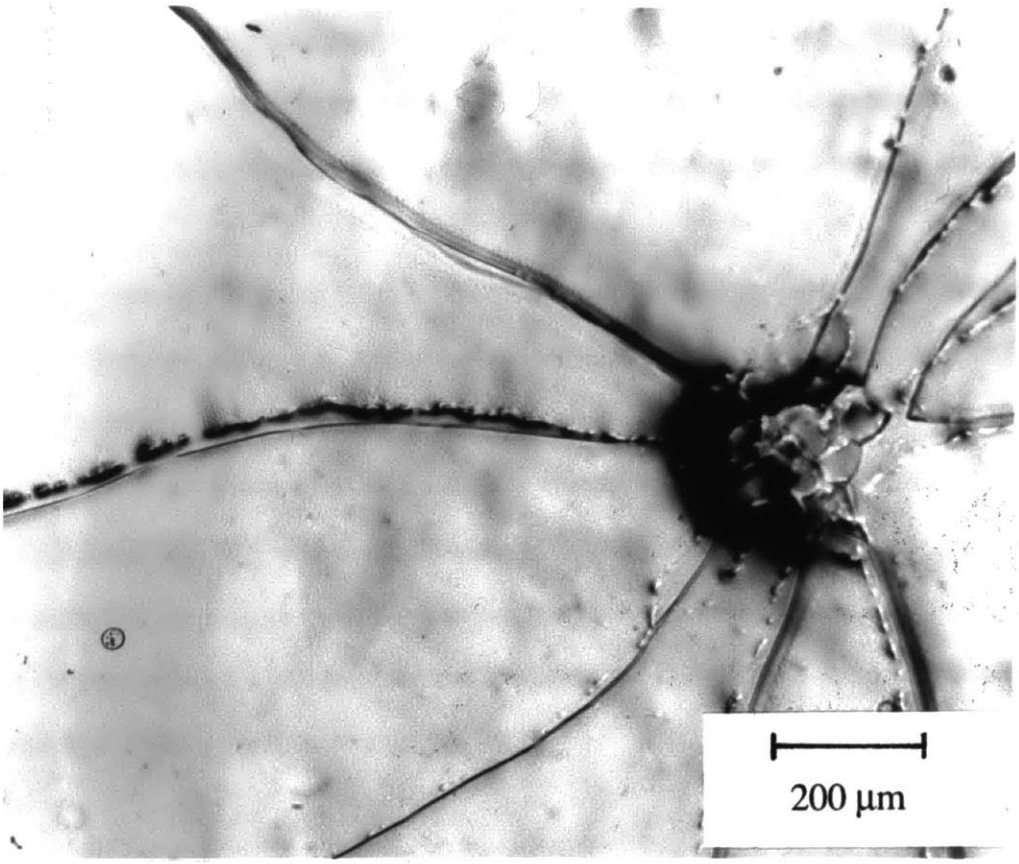

Fig. 29. Microstructure indicating that highly mobile grain boundaries drag second phase particles during the SW heat treatment (1000 °C).

that the pH of the bath used by Thompson and Saxton (33) to produce nickel strip 4-8 mm thick increased significantly. However, the oxygen content of these deposits was significantly less than that of the material produced in the present study (Table 5). Since oxygen in the deposit is believed to result from incorporation of nickel hydroxide, it appears that some other mechanism must be responsible for the microstructure obtained by Thompson and Saxton.

Other differences in the impurity concentrations of the nickel produced in the two studies can be noted in Table 5. Although the exact concentrations of sulfur and carbon are not known for the material of the present study (the levels were below the limit of detection of the LECO analyzers), they are lower than those for the material produced by Thompson and Saxton. This difference suggests that there bath was contaminated with a organosulfur compound. These materials are added in small quantities to commercial nickel electroplating baths to reduce the internal stress and increase the brightness of the deposit. A dramatic refinement of the grain size accompanies these changes (43).

6.2. Permeation Measurements

Several interesting problems associated with the input boundary condition were encountered in this study. As noted in section 5, determination of the effective diffusion coefficient from the lag time is based upon the assumption that the constant cathodic current applied to the input surface creates a constant concentration input condition. This assumption can be tested by comparing the shapes of the experimental and theoretical permeation transients. The theoretical transient is calculated from a solution to Fick's Second Law with the initial and boundary conditions described above. Several solutions have been reported in the literature (44, 45). Solution by Laplace transformation yields a power series; the early portion of the permeation transient is adequately described by the first term:

Table 5.

Compositional differences in electrodeposited nickel.

	concentration (ppm)	
impurity	present study	reference 32
oxygen	70	20
carbon	< 50	56
sulfur	< 20	26

$$i = \frac{2 L i_{ss}}{\sqrt{\pi D t}} \exp\left(\frac{-L^2}{4 D t}\right) \qquad [6]$$

where i = time-dependent permeation current density
t = time.

An experimental permeation transient produced with an electrodeposited nickel specimen (L = 47.0 μm) and a step in the cathodic current density from 0.17 to 17 mA/cm^2 is presented in Fig. 30. This curve deviates significantly from the theoretical transient corresponding to an effective diffusion coefficient of 1.4 x 10^{-12} m^2/s (the value calculated from the lag time) at short times.

A possible explanation for this discrepancy has been suggested by Pumphrey (46), who modeled permeation arising from a different type of input boundary condition. If both the forward and backward reactions associated with hydrogen absorption

$$H_{adsorbed} \underset{k_{des}}{\overset{k_{abs}}{\rightleftharpoons}} H_{absorbed} \qquad [7]$$

are considered, the corresponding input boundary condition is:

$$J_i = k_{abs}\,\theta - k_{des}\,C_o(t) \qquad [8]$$

where J_i = time-dependent flux of hydrogen into the input surface
θ = input surface hydrogen coverage.

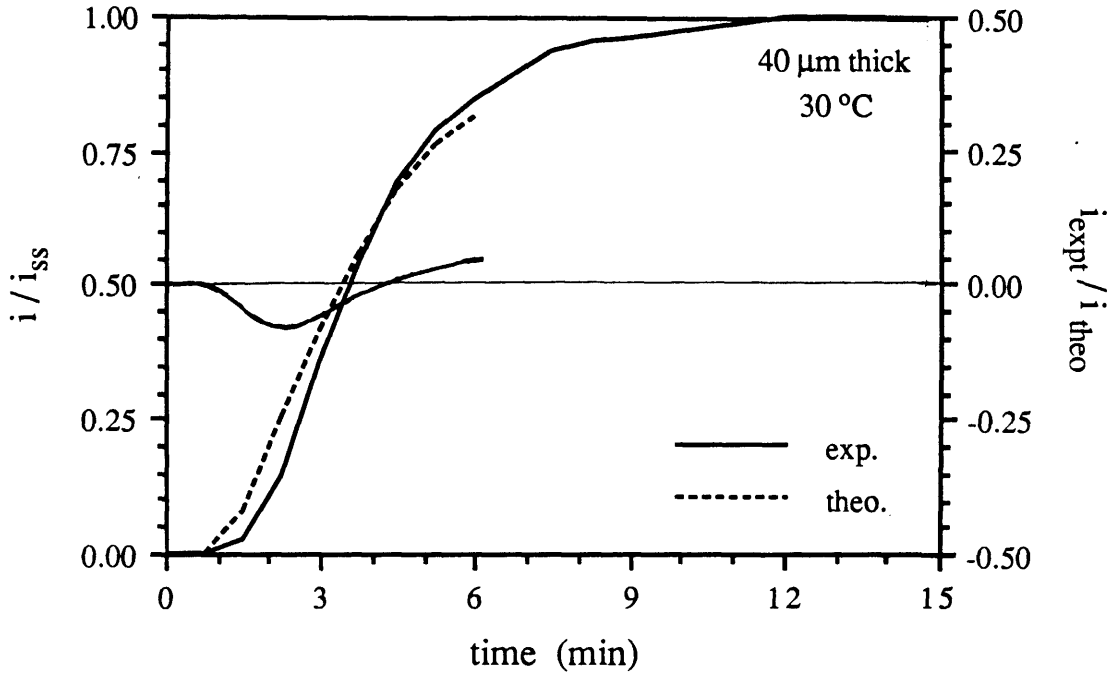

Fig. 30. Comparison of experimental permeation transient for electrodeposited nickel and theoretical transient corresponding to the lag time determined from the experimental data. Deviation from perfect fit is significant at short times.

Pumphrey assumed that galvanostatic control of the input surface produces a constant surface coverage. At steady state, C_o is also constant, and equations [4] and [8] can be combined:

$$\frac{1}{i_{ss}} = \frac{F L k_{des}}{D k_{abs} \theta} + \frac{F}{k_{abs} \theta} \qquad [9]$$

Thus, a plot of $1 / i_{ss}$ vs. L should provide ($k_{abs} \theta$) and k_{des}. Data from a wide range of specimen thicknesses are presented in this form in Fig. 31. The plot is linear, but the intercept value is negative, which is clearly unreasonable for the reciprocal of the product of a rate constant and surface coverage. However, small changes in the data can shift the intercept to positive values. This observation suggests that the factors ($k_{abs} \theta$) and (k_{des} / D) are both large, as expected. On the other hand, the negative intercept may be the result of a slight curvature in the plot, with the slope becoming less steep with increasing specimen thickness. This type of behavior has been observed by Devanathan et al. (47) with iron specimens cathodically polarized in 0.1 N H_2SO_4 (Fig. 32). No explanation for this behavior was provided. It is certainly not related to surface reaction limitation, since the shift in the data is toward higher, not lower, fluxes.

Pumphrey's model suggests that the constant concentration boundary condition is approached as the thickness of the specimen increases. In the present study, fit between experimental and theoretical transients improved with increasing specimen thickness; the two are indistinguishable with specimens exceeding 60 μm in thickness. The model also suggests that when the effective diffusion coefficient is quite small, a constant concentration input boundary condition can be produced on thin specimens. This behavior was also observed; fit to the theoretical transient was much improved with an HT-1 specimen 41.0 μm in thickness, and was perfect with an HT-2 specimen only 33.2 μm thick. Perfect fit was also noted with the VA materials.

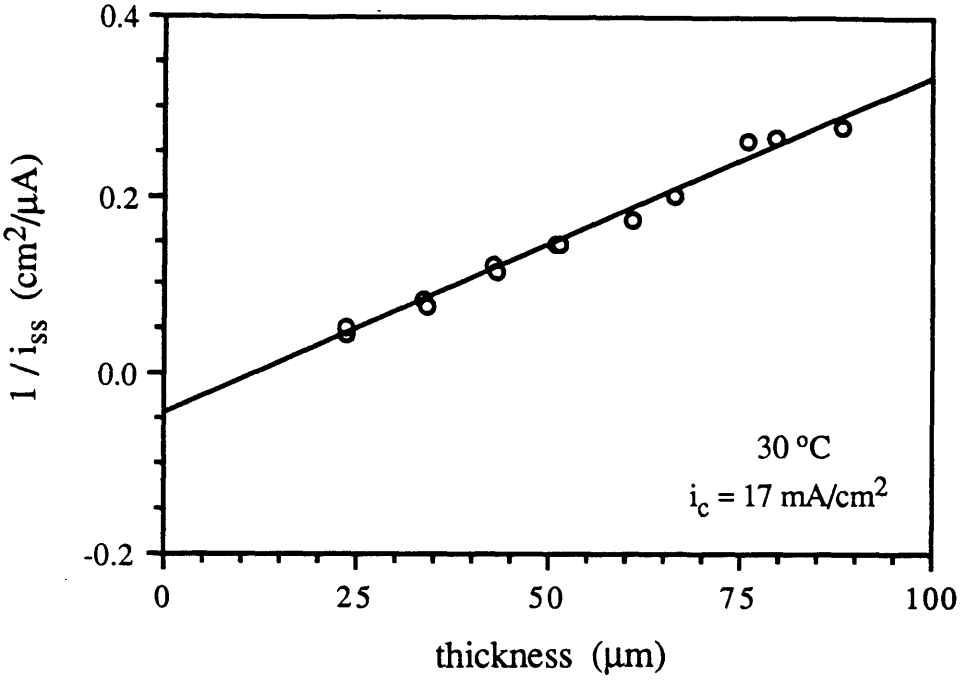

Fig. 31. Effect of specimen thickness on the steady state permeation current density for electrodeposited nickel.

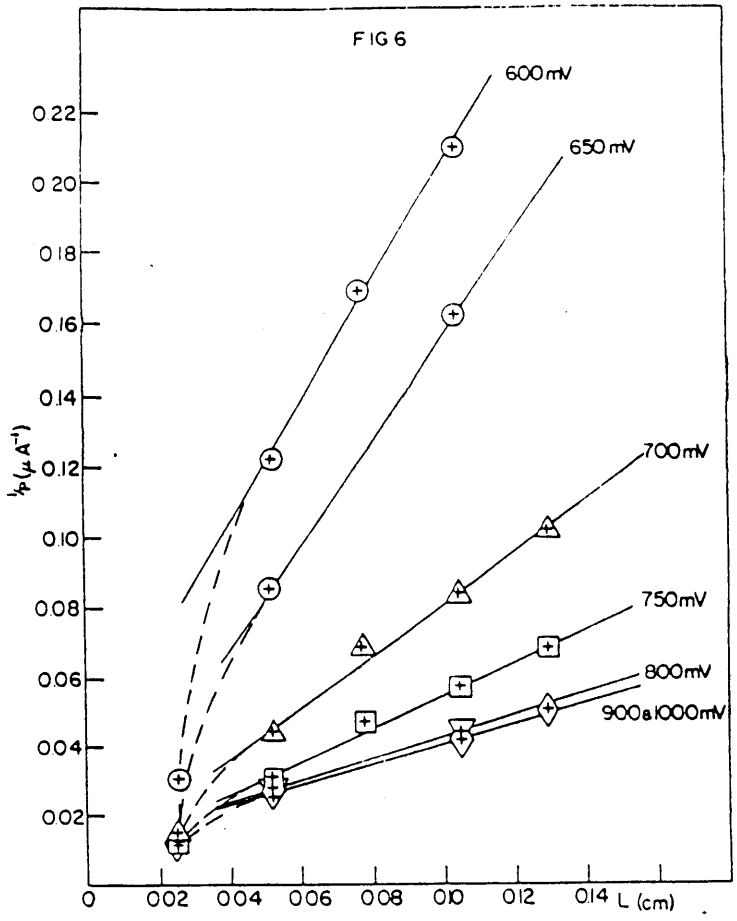

Fig. 32. Effect of specimen thickness on the steady state permeation current density for iron in 0.1 N sulfuric acid. (Ref. 47)

Since the true diffusion coefficient is calculated from the steady state permeation current density rather than the transient that precedes it, the ability to produce a constant concentration input condition at the beginning of the permeation experiment is not important to its determination. However, the ability to reproduce i_{ss} from one experiment to the next is critical. Two separate problems involving this parameter were encountered.

It can be noted in Fig. 23 that the steady state permeation current for the first transient is significantly greater than that for the second transient. The latter value was reproduced in subsequent experiments on the same specimen. This behavior was typical of all materials examined in this study. It is believed to be associated with a change in wetting of the surface that occurs with prolonged exposure to the input electrolyte. The wettability affects the adherence of hydrogen gas bubbles to the surface. This in turn influences the effective surface area of the specimen, since adhering bubbles restrict the supply of electrolyte to the surface beneath them. Since the galvanostat provides a constant current to the input surface, changes in the effective surface area will produce changes in the cathodic current density. And changes in the cathodic current density can affect the input concentration (Fig. 24).

Long term instability of the input concentration was encountered with annealed specimens. A slow but steady increase in the permeation current density was observed over long periods of cathodic polarization. A shift in the potential at the input surface to more cathodic values accompanied this behavior.

The long-term drift in the permeation current density was originally believed to arise from the growth of a hydride layer into the specimen. Hydride formation has been detected with cathodic current densities as low as 0.8 mA/cm^2 when an hydrogen evolution poison (e.g. an arsenic compound) is added to the electrolyte (48). Experiments conducted by Rommal and

arsenic compound) is added to the electrolyte (48). Experiments conducted by Rommal and Moran (8) suggest that hydride forms in alkaline electrolytes with current densities less than 25 mA/cm^2. The simplest means of checking for hydride formation in the present experiments would be to compare the input concentration corresponding to the maximum cathodic current density to the terminal solubility for hydrogen in α-nickel (i.e., the concentration of hydrogen in the solid solution that is in equilibrium with the hydride phase). Unfortunately, an accurate value for this parameter is not available. This discovery prompted the development of a method, based on the electrochemical permeation technique, for determining the terminal solubility of hydrogen in hydride-forming metals. The Appendix describes the application of this method to palladium and nickel. Although the determination of the terminal solubility proved to be more difficult in the latter case, the results clearly indicate that nickel hydride does not form under the input conditions used routinely in this study.

Further work on the long-term stability problem revealed that it is related to the specimen surface roughness, which was reduced by annealing. When the electrodeposited specimens were electropolished, the slow, steady rise in the permeation current density was again observed. This suggests that the behavior is a manifestation of contamination of the input surface with electrolyte impurities that inhibit the hydrogen evolution reaction (and, as a consequence, enhance absorption). The additional surface area provided by the matte surface of the as-deposited specimens is apparently sufficient to overcome the contamination effect. Atrens et al (29) report successful permeation measurements on annealed nickel coated with a rough electrodeposit of nickel. This approach was not investigated because of concern that the coating might contribute a significant number of hydrogen trap sites. The chemical etch described in section 4.2. proved to be a satisfactory substitute.

6.3. Analysis of Hydrogen Diffusion

Two methods for determining the diffusion coefficient from permeation data were described in section 5. The true diffusion coefficient (D) for the electrodeposited nickel averaged 3.3 x 10^{-12} m^2/s and was significantly larger than the effective diffusion coefficient (D_{eff}), which was reduced by trapping. Calculation of D (equation [4]) is based on the assumption that the relationship between the input concentration and the cathodic current density applied to the input surface (Fig. 24) is not affected by the microstructure of the nickel. The nature of the electrodeposited specimens allowed this assumption to be tested.

It was noted in section 4. that the material at the surface that had been adjacent to the anodized titanium cathode was extremely fine-grained (Fig. 7). For specimens exceeding 25 μm in thickness, the material at the other surface exhibited grains up to 2 μm in diameter in addition to fine-grained material (Fig. 9). Because of its roughness, the latter surface ordinarily served as the input surface in the permeation experiments. However, specimens tested "upside down", so that the substrate surface was cathodically polarized, exhibited permeation behavior identical to specimens tested in the usual orientation. If the microstructure at the input surface influenced the absorption of hydrogen, the two specimen orientations would provide different permeation behavior. Thus, this result supports the validity of the assumption upon which the calculation of the true diffusion coefficient is based.

The true diffusion coefficient for the electrodeposited material was calculated from permeation experiments utilizing the entire range of cathodic current densities accessible with the standard input electrolyte (see section 4.2.). A portion of these data are plotted in Fig. 33. The diffusion coefficient is independent of the cathodic current density; this relationship provides further support of the assumption discussed above.

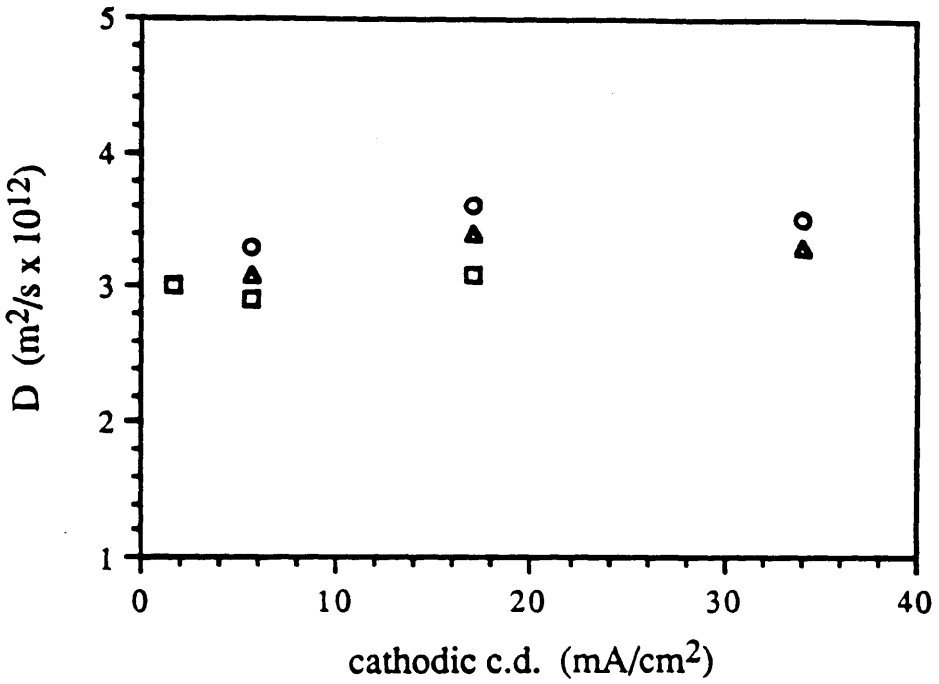

Fig. 33. Effect of cathodic current density on the true diffusion coefficient at 30 °C for hydrogen in electrodeposited nickel. Data correspond to three specimens approximately 50 μm in thickness.

The true diffusion coefficient determined with the electrodeposited nickel is more than forty times larger than that of the fully-annealed material (VA-2). This clearly indicates that grain boundary diffusion contributes to the transport of hydrogen in the former. However, the diffusion coefficient determined experimentally may still be less than the grain boundary diffusion coefficient. A short circuit diffusion model developed by Hart (49) illustrates this point. The model is based on the one-dimensional random walk problem; for lattice diffusion, it can be shown that the diffusion coefficient (D_l) is related to the mean-square diffusion distance ($\overline{X^2}$) by the expression (50):

$$\overline{X^2} = 2 D_l t \qquad [10]$$

where t = time.

Hart modified the random walk problem to include the interaction of a diffusing atom with dislocations. The atom remains in the vicinity of a dislocation for a mean time τ, during which it migrates over the mean-square projected distance $\overline{l^2}$. The overall mean-square migration distance ($\overline{S^2}$) thus becomes:

$$\overline{S^2} = n \overline{l^2} + \overline{X^2} \qquad [11]$$

where n = number of times the diffusing atom encounters a dislocation.

The number of atom-dislocation encounters is defined by the expression:

$$n = \frac{f t}{\tau} \qquad [12]$$

where f = fraction of all metal atoms in dislocations.

Substituting equation [12] into [11] and rewriting each term in the form equation [10], equation [11] reduces to:

$$D = \frac{\overline{l^2} f}{2\tau} + D_l (1-f) \qquad [13]$$

where D = the experimentally determined diffusion coefficient.

Hart noted that the quantity $(\overline{l^2}/2\tau)$ is roughly equivalent to the dislocation diffusion coefficient.

It would appear that this expression is readily applicable to the case of grain boundary diffusion of hydrogen in nickel. However, the Hart model pertains to self-diffusion. In general, grain boundary self-diffusion models are extended to the case of solute diffusion by multiplying the grain boundary diffusion coefficient with a segregation coefficient (s), which relates the solute concentration at the grain boundaries (C_b) to that inside the grains (C_l):

$$s = \frac{C_b}{C_l} = \exp\left(\frac{E_b}{R T}\right) \qquad [14]$$

where E_b = binding energy of the solute to an average grain boundary trap site
R = gas constant
T = absolute temperature.

Thus, the Hart equation for the present system is:

$$D = D_b s f + D_l (1-f) \qquad [15]$$

where D_b= grain boundary diffusion coefficient.

Superficially, the use of a segregation coefficent in an expression for the true diffusion coefficient presents a contradiction. It was stated in section 5. that trapping does not affect steady state permeation, and therefore, D. A more precise statement is that steady state permeation is not reduced by trapping. However, if the overall flux of hydrogen is enhanced by grain boundary diffusion, and grain boundary diffusion is enhanced by trapping, then trapping can increase steady state permeation. In terms of the Hart model, this effect is realized through an increase in the mean-square projected distance ($\overline{l^2}$) the hydrogen atom migrates in the grain boundary each time one is encountered.

Equation [15] is readily solved for the grain boundary diffusion coefficient if s and f can be determined. With respect to the first parameter, the choice of a binding energy is most important. As noted in section 5, trapping is evident from the hydrogen permeation behavior of the electrodeposited nickel. A quantitative analysis of the trapping is presented is in the next section. The binding energy of the dominant trap site is nearly 30 kJ/mol, a value significantly larger than those for grain boundaries determined in previous studies (1, 25). Thus, it was concluded that trap sites in the electrodeposited nickel are associated with solute atoms or very small second phase particles, which may or may not be located at the grain boundaries. Since only those trap sites that are located in the vicinity of the grain boundaries will enhance grain boundary diffusion, the binding energy above is not appropriate for use in equation [14].

Lee and Lee (25) have determined the binding energy for hydrogen to grain boundaries in nickel to be 20 kJ/mol. Their samples were commercially-pure nickel (Ni 270) of moderate grain size. The grain boundaries of this material may have been contaminated with solutes that

increase the susceptibility to hydrogen embrittlement (26), suggesting that the segregation of hydrogen may have been enhanced by their presence. With high-purity nickel, Lassila and Birnbaum (1) determined the binding energy to be 11.6 kJ/mol. However, the grain size of their specimens was very large, a condition that promotes grain boundary contamination (26). The composition of the grain boundaries in the electrodeposited nickel of the present study was not assessed directly, but the total impurity concentration is low and the total interfacial area is high. This suggests that the concentration of impurities at the grain boundaries in this material is low, even if the impurity atoms are preferentially deposited at the grain boundaries by the electroplating process. Thus, a reasonable value of the binding energy for hydrogen segregation to grain boundaries in the electrodeposited nickel is 10 kJ/mol. At 30 °C, this value corresponds to a segregation coefficient of 53.

The volume fraction of grain boundary material can be defined as the product of the grain boundary area per unit volume (S_v) and the grain boundary thickness. The former is related to the mean linear intercept ($\bar{l}$) by the expression (51):

$$S_v = \frac{2}{\bar{l}} . \qquad [16]$$

Unfortunately, $\bar{l}$ was difficult to determine for the electrodeposited nickel because of its inhomogeneous microstructure (see section 4.1.). However, if grain boundary diffusion does contribute to the overall transport of hydrogen, then permeation through the fine-grained regions may dominate that through the rest of the specimen. The mean linear intercept for this material is estimated to be less than 100 nm, although the grain boundaries were difficult to resolve by TEM, even at higher magnification (Fig. 10).

The thickness of the grain boundary (δ) should relate to the distance from the grain boundary

plane at which the distortion of the lattice is no longer sufficient to provide enhanced diffusion. A value of 0.5 nm is frequently used in studies of grain boundary diffusion of substitutional solutes. The report of extended deuterium segregation to nickel surfaces by Fukushima and Birnbaum (23) suggests that the grain boundary thickness for hydrogen diffusion may be greater than 0.5 nm, since any distortion of the crystal structure that would promote segregation can be imagined to provide short-circuit diffusion pathways as well. Through a comparison of hydride formation in two samples with widely different grain sizes, Mutschele and Kirchheim (52) determined the average grain boundary width in palladium to be approximately 1 nm . Since this value specifically relates to the solute hydrogen, and nickel is similar in structure to palladium, it appears to be appropriate for the present calculation.

With the values of $\bar{l}$ and δ discussed above, the volume fraction of grain boundary material in the electrodeposited nickel is estimated to be 0.02. This value effectively cancels that of the segregation coefficient (at 30°C) in equation [15]. Therefore, the experimentally determined diffusion coefficient appears to be a good approximation of D_b at 30°C.

Other grain boundary diffusion models are also applicable to hydrogen permeation data. Harrison (53) has separated the behavior of these systems into three regimes, based on the extent to which lattice diffusion influences material transport in the grain boundaries. The three regimes are illustrated for the case of parallel grain boundaries in Fig. 34 (54). Type A behavior, in which $D_b < 100 \cdot D_l$, applies to hydrogen in nickel. The key feature of this case is the overlapping of the diffusion fields of adjoining grains due to extensive lattice diffusion that occurs relative to diffusion in the grain boundaries (which are represented as slabs of material characterized by a larger diffusion coefficient). A solution to the differential equations describing type A behavior in a sample of infinite thickness has been derived by Campbell

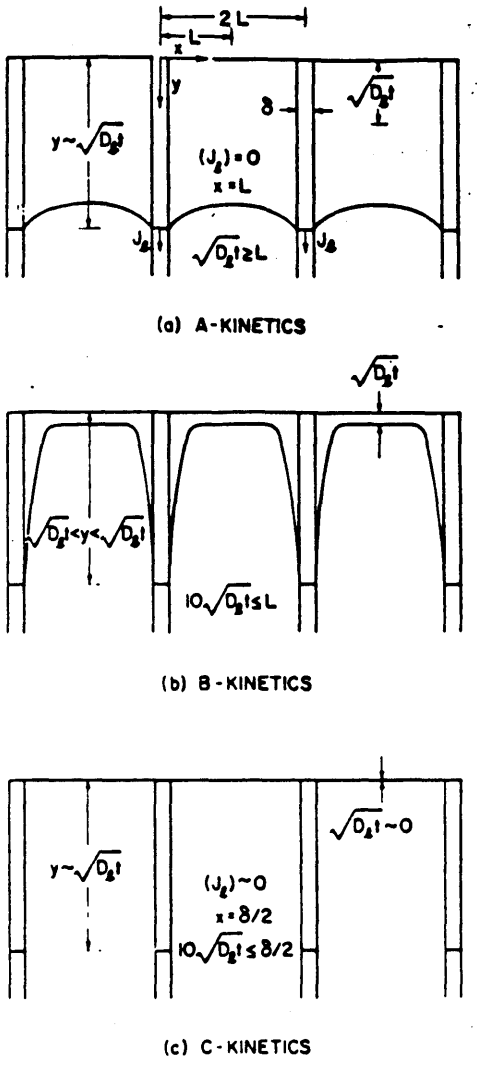

Fig. 34. Illustration of concentration profiles resulting from solute transport by both grain boundary and lattice diffusion. (Ref. 54)

(55) through the use of Fourier-Laplace transforms. The behavior of this system is most clearly represented as concentration profiles corresponding to various values of the dimensionless diffusion distance Λ:

$$\Lambda = \frac{l}{2\sqrt{D_l t}} \qquad [17]$$

As Λ decrease below 0.5, lateral diffusion of material away from the grain boundaries is so extensive that the diffusion front becomes planar, and solute penetration is a function of D_b only. While a direct comparison between this model and the permeation experiments conducted in the present study is not possible (the boundary conditions are different), one can substitute values of l and t into [17] to assess the extent to which diffusion into the interior of the grains lags behind the penetration of hydrogen along the grain boundaries. With t = 60 sec (the breakthrough time for an electrodeposited specimen greater than 60 μm in thickness), a mean linear intercept of 2 μm provides a Λ value of 0.46. Since few grains in the electrodeposited specimens exceed 2 μm in diameter, this result also suggests that the measured value of the diffusion coefficient equals the grain boundary diffusion coefficient.

As noted in section 5, the temperature dependence of the true diffusion coefficient determined with the electrodeposited nickel appears to be significantly different from that of the same material after annealing (Table 4). However, the temperature range over which permeation was measured is too narrow to justify much confidence in this result. One means of reducing the uncertainty in this determination is to assume that the y-axis intercept in the Arrhenius plot (D_0) is the same for both lattice and grain boundary diffusion. Through a semiempirical method, Zener (56) has shown that this quantity is approximated by the expressions:

$$D_o \cong \gamma a_o^2 \nu \exp\left(\frac{\beta \Delta H}{R T_{mp}}\right) \qquad [18]$$

$$\beta \equiv -\frac{d(\mu/\mu_o)}{d(T/T_{mp})} \qquad [19]$$

where γ = geometric factor
a_o = jump distance
ν = frequency with which the solute atom vibrates in the diffusion direction
ΔH = activation enthalpy for diffusion
T_{mp} = melting point of the pure metal
μ = elastic modulus of the pure metal
μ_o = elastic modulus at zero degrees absolute.

None of the parameters above change substantially with the distortion of the lattice associated with a general grain boundary. Thus, D_o should be roughly the same regardless of whether solute transport is dominated by lattice or short circuit diffusion.

When the least squares fit of the grain boundary diffusion data (Fig. 35) is forced through the "best" D_o value for lattice diffusion determined by Robertson (20), an activation energy of 30 kJ/mol for the former is obtained. This value is only slightly smaller than the activation energy for grain boundary diffusion determined by Kimura and Birnbaum (17). Both values are approximately 25% less than the activation energy for lattice diffusion; the temperature dependence of the latter (20) is included in Fig. 35 for comparison.

It is interesting to note that the modified Hart model discussed above offers an explanation for the low activation energy value (14 kJ/mol) determined from Fig. 26. With a binding energy of 10 kJ/mol, an increase in the temperature from 30 to 72 °C (the highest temperature utilized in the present study) reduces the segregation coefficient (equation [14]) by nearly 50%. This behavior should produce a corresponding decrease in the experimentally determined diffusion coefficient (equation [15]). Thus, the slope of the Arrhenius plot over the experimental

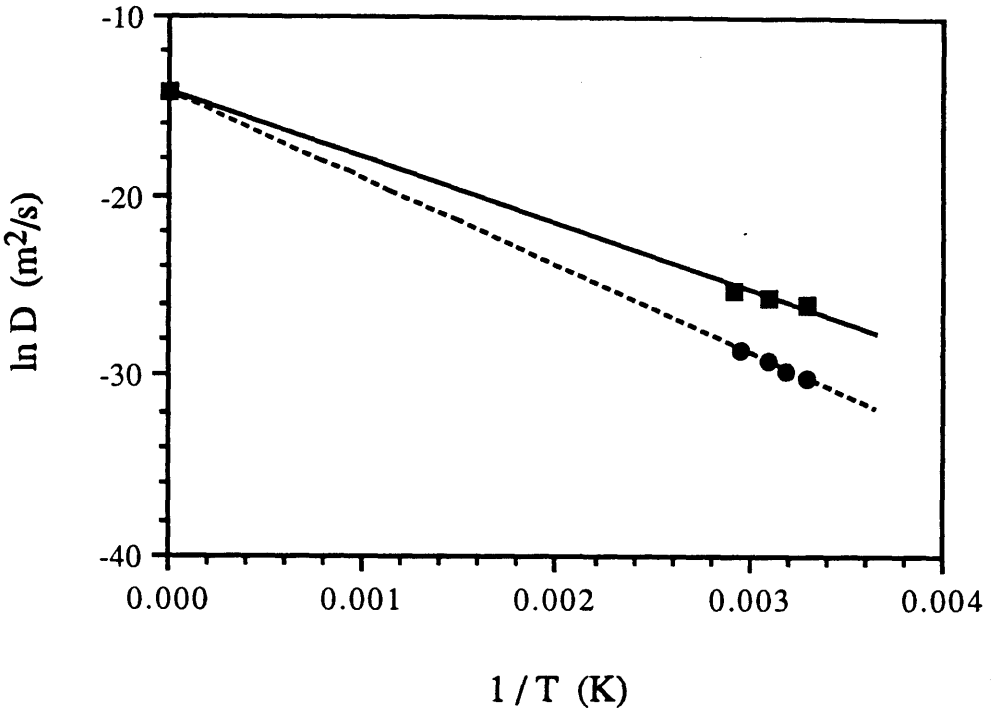

Fig. 35. Arrhenius plot of diffusion data. The dashed line represents the "best" temperature dependence of lattice diffusion determined by Robertson (20). The closed circles represent data from the VA-2 material. The closed boxes represent diffusion data from the electrodeposited nickel. The solid line is the least-squares fit of the electrodeposited nickel data forced through the y-axis intercept for lattice diffusion.

temperature range reflects the temperature dependence of two different (but related) processes. By forcing the least squares line to pass through a reasonable value of D_0, the effect of trapping on the activation energy is greatly reduced.

6.4. Analysis of Hydrogen Trapping

As expected, based on the work of Mutschele and Kirchheim (6), the effective diffusion coefficient determined with the electrodeposited nickel is influenced by the specimen's initial hydrogen content (see section 5.). An increase in the initial hydrogen concentration also resulted in a larger D_{eff} (Fig. 36). The use of current densities in excess of 34 mA/cm^2 required an increase in the salt concentration of the electrolyte in order to limit Joule heating (22).

These data has been analyzed with a model developed by McNabb and Foster (32) to treat saturable (limited occupancy) hydrogen traps. Johnson et al. (57) have shown explicitly that for saturable traps, the lag time should decrease with increasing input hydrogen concentration (or the corresponding cathodic current density). Since the lag time is inversely related to the effective diffusion coefficient (see equation [3]), Fig. 36 clearly indicates that the hydrogen traps in electrodeposited nickel are saturable.

The McNabb-Foster model is based on probability considerations. The rate of trapping is proportional to the lattice concentration and the fraction of unoccupied traps, while the rate of escape is dependent only on the fraction of occupied traps:

$$\frac{dn}{dt} = k C_l (1 - n) - p\ n \qquad [20]$$

where n = fractional occupancy of traps

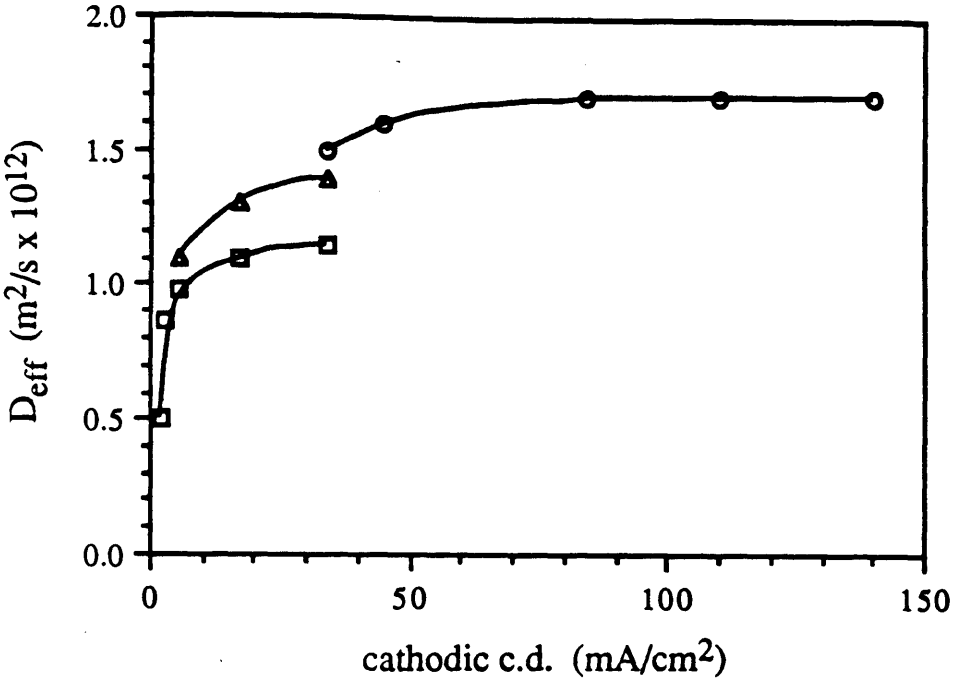

Fig. 36. Effect of cathodic current density on the effective diffusion coefficient at 30 °C determined with electrodeposited nickel specimens. Squares denote data corresponding to the initial condition produced with a cathodic current density (i_c) of 0.17 mA/cm^2. Triangles denote the initial condition produced with i_c = 1.7 mA/cm^2. Circles denote initial condition corresponding to i_c = 1.7 mA/cm^2, and the use of concentrated electrolyte.

k = transition probability for hydrogen to jump from the lattice to the trap site

C_l = lattice hydrogen concentration

p = transition probability for hydrogen to jump from the trap site to an adjacent lattice site.

The transition probabilities can also be expressed in terms of the thermal activation concept:

$$\frac{k}{p} = \frac{1}{N_l} \exp\left(\frac{E_b}{R\,T}\right) \qquad [21]$$

where N_l = concentration of lattice sites for hydrogen.

For the initial and boundary conditions used in the present study, an exact solution for the lag time (t_L) could be determined (32):

$$t_L = t_o \left\{ 1 + \frac{3\alpha}{\beta} + \frac{6\alpha}{\beta^2} + \frac{6\alpha}{\beta^3}(1+\beta)\ln(1+\beta) \right\} \qquad [22]$$

where t_o = lag time corresponding to pure lattice diffusion

$\alpha = N_t\, k / p$

N_t = trap site density

$\beta = C_o\, k / p$.

Two limiting cases of equation [22] have been identified by Johnson et al (57). In the regime of dilute occupancy (β,n << 1):

$$\frac{t_L}{t_o} - 1 = \alpha. \qquad [23]$$

In the regime of trap saturation ($n \cong 1$, $\beta >> 1$):

$$\frac{t_L}{t_o} - 1 = \frac{3\alpha}{\beta} = \frac{3 N_t}{C_o} \qquad [24]$$

The form of equation [24] suggests that a plot of $[(t_L / t_o) - 1]$ vs. $(1 / C_o)$ would assist in the analysis of the data. A schematic diagram of this plot (58) is presented in Fig. 37.

As noted in section 5., the input concentration produced by a particular cathodic current density applied to the input surface (i_c) of an electrodeposited specimen was determined indirectly, through permeation measurements on the VA-2 material. This allowed the true diffusion coefficient to be determined from the steady state permeation current density with equation [4]. The lag time corresponding to the true diffusion coefficient (t_o) could then be calculated with equation [3].

With the estimated values of t_o and C_o, the permeation data for electrodeposited nickel could be analyzed for trapping as described above. First, the shortest lag time obtained from a series of permeation transients produced with various values of i_c was used to solve equation [18] for the trap site density. Ordinarily, this lag time corresponded to a step in the cathodic current density from 0.17 to 17 mA/cm^2. Since it can be inferred from Fig. 36 that a shorter lag time may be obtained (through the use of a more concentrated electrolyte), the use of this particular value of t_L will result in an overestimate of the trap site density. On the other hand, using an initial condition corresponding to i_c = 0.17 mA/cm^2 provides a much shorter lag time than would be obtained with the zero concentration initial condition (compare tansients **a** and **b**, Fig. 23).

Despite the uncertainty associated with the determination of the trap site density, an accurate value of the binding energy can still be obtained. Permeation data for electrodeposited

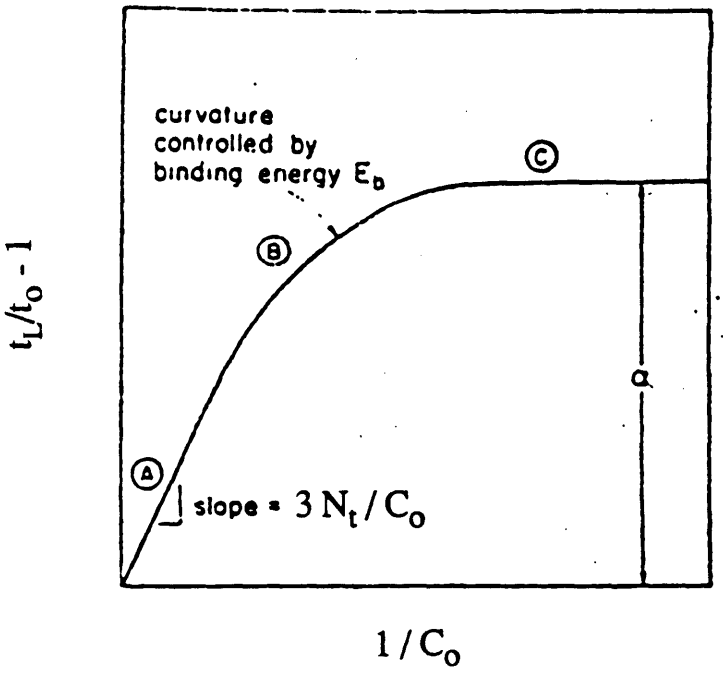

Fig. 37. Relationship between input hydrogen concentration and the trapping parameter $[(t_L/t_o) - 1]$. (Ref. 58, but symbols have been changed to be consistent with the present document)

specimens are plotted according to equation [16] in Fig. 38. It can be noted that in the regime of dilute trap occupancy, the experimental data fall between the curves corresponding to binding energies of 28 and 30 kJ/mol. A binding energy of 29 kJ/mol is significantly larger than previously reported values for grain boundary segregation of hydrogen in nickel. The largest of these, 20.5 kJ/mol (25), was determined with material containing tin and antimony at the grain boundaries (26), which probably enhanced the segregation of hydrogen.

Robertson (59) has examined hydrogen trapping at incoherent phase boundaries in nickel. The second phase was thoria, in the form of spherical particles with an average diameter of 22 nm. The binding energy was determined to be 30 kJ/mol, which is in good agreement with the values determined in the present study. This would suggest that trapping in the electrodeposited nickel may be due to extremely small second phase particles, most likely containing oxygen, since it is the most plentiful impurity. However, second phase particles are not evident in TEM micrographs of electrodeposited nickel produced on a clean cathode (Figs. 7-10).

With respect to the number of ordinary octahedral interstices per cubic meter of a perfect crystal of nickel, a trap site density of 4×10^{18} cm^{-3} corresponds to a trap site / lattice site ratio of 4×10^{-5}, or 40 ppm. It may be recalled that the bulk concentration of oxygen in the electrodeposited material is 70 ppm. This suggests that the trap sites that dominate this system may simply be dissolved oxygen atoms. Since it is unknown whether the electrodeposition process localizes oxygen or other solutes to the grain boundaries, the dominant trap sites may not even be associated with the grain boundaries.

The permeation behavior of the heat-treated materials was much less dependent on the initial hydrogen content. Permeation data for the HT-1 and HT-2 materials were also analyzed with

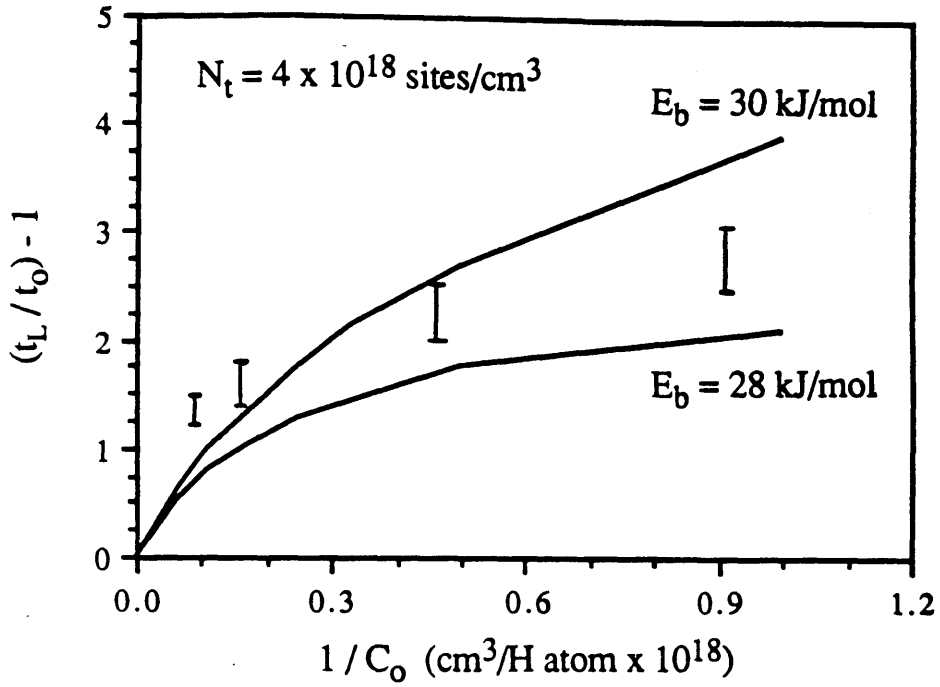

Fig. 38. Relationship between input hydrogen concentration and the trapping parameter $[(t_L/t_o) - 1]$. Curves denote theoretical relationships corresponding to a trap site density of 4×10^{18} cm^{-3} and two different binding energies. Experimental data are denoted by error bars.

the McNabb-Foster model. Values for the binding energy and trap site density are listed in Table 7. The binding energy remained relatively constant, but the trap site density decreased with higher annealing temperatures. Second phase particles are visible in well-annealed specimens (Figs. 13-15). These observations are consistent with a change in the dominant trap site from individual solute atoms to the phase boundary surrounding each second phase particle. Coarsening reduces the phase boundary area, and with it the overall number of trap sites. In the case of the VA-2 material, the number of trap sites is too small to detect by permeation measurements.

It is conceivable that the number of trap sites associated with grain boundaries in electrodeposited nickel far outnumbers the trap site density determined above. Why, then, do these defects go undetected? This appears to result from an inherent flaw in trapping analyses for permeation data: they are sensitive only to the deepest saturable trap sites, regardless of their number or the number of sites corresponding to smaller binding energies. When Kumnick and Johnson (58) applied the model to the trapping of hydrogen at dislocations in iron, they obtained a binding energy that was nearly a factor of two greater than that obtained by other techniques.

6.5. Grain Boundary Diffusion of Hydrogen and the Embrittlement of Metals

To complete the discussion, the impact of these results on the embrittlement of metals should be considered. It was noted in the introduction that stage II crack growth rates for iron and nickel are similar (2), suggesting that the rate of hydrogen transport to grain boundaries in these two materials is similar. However, the analysis of hydrogen diffusion in the previous section indicates that the maximum grain boundary diffusion coefficient (i.e. with completely saturated traps) for nickel probably does not exceed 5×10^{-12} m^2/s. This value is still

Table 7.

Hydrogen trapping in electrodeposited and annealed nickel.

material	binding energy (kJ/mol)	trap site density (cm^{-3})
electrodeposited	29	4×10^{18}
HT-1	28	1×10^{18}
HT-2	28	3×10^{17}

significantly smaller than the effective diffusion coefficient for hydrogen in steel. Thus, it appears that the transport of hydrogen well ahead of the crack tip may not be necessary for embrittlement. Instead, hydrogen transport in the process zone immediately ahead of the crack tip, which could occur by dislocation transport as well as grain boundary diffusion, appears to be the most important issue. This concept could be tested through fracture mechanics tests in which the plastic zone size, the grain size and the hydrogen content are independently controlled.

The analysis above could be applied to other metals if their grain boundary difusion coefficients were known. Unfortunately, the investigation of grain boundary diffusion in fine-grained palladium (6) reviewed in the introduction constitutes the only study not involving nickel. With this metal, the maximum effective grain boundary diffusion coefficient was only eight times greater than the lattice diffusion coefficient at room temperature. Since lattice diffusion is much greater in palladium than in nickel, it would appear that the importance of grain boundary transport correlates with the difficulty of lattice diffusion. This hypothesis could be tested through experiments with aluminum or titanium, both of which are embrittled by hydrogen and exhibit slow lattice diffusion.

Finally, it should be noted that the trapping of hydrogen in the electrodeposited nickel may also be of interest to the embrittlement community. The binding energy of the dominant trap sites in this material, which appear to be associated with dissolved oxygen atoms or very small oxygen-containing second phase particles, is equivalent to that determined for thoria particles dispersed in nickel (59). Thompson and Wilcox (60) have demonstrated that thoria-dispersed nickel is considerably more resistant to embrittlement than commerically-pure nickel in the straining electrode test (the tensile specimen is cathodically polarized during straining). They attributed this result to the competition between trap sites; the phase boundaries, exhibiting a greater affinity for hydrogen than the grain boundaries, actually reduce the segregation of

hydrogen to the grain boundaries, thereby reducing the extent of embrittlement. Robertson (59) has also demonstrated that the trap site density associated with thoria particles increases as the material is cold-worked. If the same behavior occurs when hydrogen is present in the material during plastic straining, then hydrogen transport from grain boundary trap sites to those in the phase boundaries may be an important issue with respect to embrittlement. The greater number of grain boundaries in the electrodeposited material should enhance the rate at which hydrogen redistributes from one trap site to another. Thus, electrodeposition may represent the best means of processing nickel to provide both a fine grain size and strong trap sites associated with oxygen.

7. Conclusions

1. Thin nickel foil suitable for permeation measurements was produced with an electrolyte based on the sulfamate salt of nickel and a reusable anodized titanium cathode. The deposits contained no through-thickness pinholes when the cathode surface was free of atmospheric particulates. Closed-off pinholes were limited in depth to a small fraction of the specimen thickness.

2. Each electrodeposited specimen exhibited a wide range of grain sizes. The average grain diameter at the surface that had been adjacent to the cathode was less than 0.1 μm. As the deposit thickened, the microstructure evolved into a mixture of the fine-grained material and distinct grains up to 2 μm in diameter.

3. Grain growth occurred in the electrodeposited material with annealing. With temperatures up to 600 °C, the growth was primarily limited to the fine-grained material, so that the grain size distribution narrowed substantially. Second phase particles formed with annealing at 800°C. Abnormal grain growth was observed in specimens annealed at 1000°C.

4. Hydrogen permeation in the electrodeposited nickel was clearly dependent on both the initial concentration of hydrogen in the specimen and the input concentration produced by the cathodic current density applied to the input surface. This behavior suggests that there are a significant number of trap sites for hydrogen in the material. The effective diffusion coefficient determined from the transient in the permeation current density was reduced by the trapping.

5. Hydrogen permeation in fully annealed specimens (heat treatment VA-2) is controlled by lattice diffusion. The diffusion coefficient at 30°C, 7.8 x 10^{-14} m^2/s, and the activation energy for diffusion, 41 kJ/mol, are in agreement with the results of previous studies conducted at higher temperatures, where trapping at crystalline defects has a negligible effect on hydrogen diffusion.

6. The negligible trapping exhibited by the fully annealed material allowed the relationship between the input concentration (C_o) and the cathodic current density applied to the input surface (i_c) to be determined. Assuming that this relationship also holds for the electrodeposited nickel, the true diffusion coefficient for this material could then be determined from the steady state permeation current density. At 30 °C, this value averaged 3.3 x 10^{-12} m^2/s.

7. Analysis of hydrogen diffusion in the electrodeposited nickel using the Hart model suggests that grain boundary diffusion in the fine-grained material throughout the specimen dominates the overall rate of hydrogen transport, and that the experimentally determined diffusion coefficient is a good approximation of the grain boundary diffusion coefficient at 30°C.

8. The temperature dependence of the true diffusion coefficient was determined over the temperature range 22-72 °C (after first determining the relationship between C_o and i_c with the fully annealed material over the same range of temperatures). The activation energy for diffusion determined from an Arrhenius plot of the experimental data was 14 kJ/mol. When the least squares fit of this data was forced through the y-axis intercept (D_o) of the lattice diffusion data (suggested by Zener as a means of reducing the uncertainty of diffusion data collected over a narrow

temperature range), the activation energy was 30 kJ/mol. This value is only slightly smaller than that determined by Kimura and Birnbaum using a fracture-based technique, and is 75% of the activation energy for lattice diffusion of hydrogen in nickel. The Hart model suggests that the low activation energy value obtained without the use of D_0 results from the effect of temperature on the binding energy of hydrogen to trap sites in the grain boundaries.

9. Analysis of the hydrogen permeation data for the electrodeposited nickel using the McNabb-Foster model provided a trap binding energy of 29 kJ/mol, which is three times larger than the previously-reported value for hydrogen segregation to grain boundaries in high-purity annealed nickel (11.6 kJ/mol), but roughly equal to the value corresponding to trap sites in the phase boundaries of thoria particles (30 kJ/mol). The trap site density was 4×10^{18} cm^{-3}, which is approximately equal to the concentration of oxygen in the deposit (70 ppm). This suggests that the trap sites are not associated with clean grain boundaries, but rather dissolved oxygen atoms or very small oxygen-containing second phase particles. The binding energy was constant with annealing, but the trap site density decreased. This behavior is consistent with trapping at the second phase particles that precipitate and/or coarsen with annealing at higher temperatures.

10. In conjunction with published data on the crack propagation of cathodically-polarized iron and nickel, the results of the present study suggest that the transport of hydrogen well ahead of the crack tip is not necessary for embrittlement. Instead, hydrogen transport in the plastic zone of the crack tip, which can occur by either dislocation transport or grain boundary diffusion, appears to be the critical issue. However, the relative importance of grain boundary diffusion may be greater with

materials that exhibit extremely slow lattice diffusion (e.g. titanium, aluminum and their alloys).

8. Suggestions for Future Work

There are several logical extensions to the work described above. While it does not appear possible to electrodeposit "pure" nickel with an average grain size less than 0.5 μm, alloys with extremely fine grains can be produced. The one method of grain refinement which would appear to hold the most promise involves the solute phosphorus. The addition of increasing amounts of phosphoric and phosphorous acids to the Watt's bath results in a steady decrease in the grain size (61). Since this bath is more acidic than the Watt's bath (or the sulfamate bath used in the present study), the incorporation of oxygen into the deposit is less likely. However, the amount of hydrogen codeposited with the nickel increases steadily with decreasing pH; this may result in deposits with high internal stress, or the formation of hydrogen gas-containing blisters at the deposit-substrate interface. If a sacrificial substrate (e.g. copper foil) must be used, a preliminary investigation of pinhole formation must be undertaken. Phosphorus is incorporated into the nickel deposited from phosphorous acid-containing baths; the solute is homogeneously distributed despite exceeding its solubility limit. Dissolved phosphorus atoms may be weak trap sites for hydrogen (62); thus, the trapping parameters may be accessible through permeation measurements and the McNabb-Foster analysis.

Of course, electrodeposition is not the only means of producing microcrystalline nickel. A parallel study using vapor deposited nickel would be quite interesting. Recently, Hirvonen et al (63) have studied hydrogen permeation through 175 nm of nickel deposited onto a 100 nm-thick layer of titanium, which reacted with the hydrogen to form a hydride. The hydride was then detected by forward recoil spectroscopy. While this method would seem to be quite clever, it suffers from an inability to test for the presence of pinholes or other macroscopic defects that could allow an inordinate amount of hydrogen to reach the titanium underlayer. It

can be concluded from the present study that hydrogen permeation is best measured in free-standing foils that are thick enough to allow a constant concentration input boundary condition to be established. The preparation of such specimens by vapor deposition would require a large amount of high-purity nickel, which is quite expensive. Furthermore, the vapor deposition unit must provide for the removal of the heat of crystallization from the specimens, or grain growth will occur as the deposit thickens (64).

Finally, the mechanical behavior of hydrogen-charged electrodeposited nickel should be evaluated. As noted in section 6.5, it is conceivable that the electrodeposited material produced in the present study will have greater resistance to embrittlement. It also appears that this material would provide better specimens for the fracture-based kinetics experiments developed by Birnbaum and his coworkers (see section 2). The ability to vary the grain size over two orders of magnitude would test the validity of the experimental results using well-annealed nickel that have been reported (1, 16, 17).

9. Appendix

A preliminary study of hydrogen permeation in palladium was undertaken with two objectives in mind. First, a coating of palladium on the input surface can improve the reproducibility of the input boundary condition (65-67). It was hoped that this approach could be used to resolve the issue of whether grain size affects the absorption of hydrogen at the input surface of a permeation specimen. Second, a study by Bowker and Piercy (67) suggests that hydride formation can be studied using the electrochemical permeation technique. The possibility of hydride formation on the input surface of the nickel specimens was a concern in the present study, particularly since the cathodic current densities employed are higher than those used in previous studies. When the literature on nickel hydride was reviewed, it was discovered that an accurate value of the terminal solubility (i.e., the α phase equilibrium concentration) has not been published. Thus, an effort was made to develop a universal method for determining the terminal solubility in hydride-forming metals and alloys, through the use of the model material palladium.

The electrochemical permeation measurements were conducted in a cell similar to that described in section 4.2. However, since much less hydrogen gas is produced at the input surface of a palladium specimen, the cell featured a vertically-oriented specimen. Furthermore, there was no need for additional O-rings to eliminate the dead volume in the O-ring fittings. Both chambers of the cell were filled with 0.1 N NaOH, which was continuously bubbled with nitrogen gas. Sufficient temperature control was achieved by submerging the lower portions of both chambers in a constant temperature bath. The output surface was anodically polarized to -0.20 V_{SCE}. To commence hydrogen permeation, a constant cathodic current was applied to the input surface.

Palladium of >99% purity was obtained from Johnson-Matthey, in the form of cold-rolled foils less than 150 μm thick. When the specimens were tested in the as-received condition, small cathodic currents applied to the input surface resulted primarily in the evolution of H_2. Vacuum annealing of the foils (800 °C for 2 hours) allowed much more of the hydrogen to be absorbed by the palladium. Specifically, the steady-state permeation current (i_{ss}) was approximately 96% of the cathodic current (i_c). This result is in agreement with that of Early (68).

The high absorption efficiency (defined as i_{ss}/i_c) afforded by vacuum annealing deteriorated over time, apparently as the result of contamination of the input surface by impurities in the electrolyte. Abrasion of the surface returned the absorption efficiency to its original value, but only for a short time. Etching of the surface with aqua regia (a 3:1 mixture of hydrochloric and nitric acids) increased the absorption efficiency to 1.00. This treatment also provided an input surface that was resistant to contamination. Thus, the aqua regia etch became a standard part of specimen preparation.

With higher values of i_c, the attainment of an absorption efficiency of 1.00 was significantly delayed (compare transients **a** and **b** in Fig. 39). If sufficient time was allowed for the steady state to be attained, a further increase in i_c always produced another transient in the permeation current (transient **c**, Fig. 40).

The quantity of hydrogen dissolved in the specimen at any time could be determined by polarizing both surfaces to -0.20 V_{SCE} (using separate potentiostats), integrating the two decay current transients resulting from the new input boundary condition, and dividing by Faraday's constant. A radical change in the hydrogen content accompanied the transition in permeation behavior described above. With low values of i_c, the amount of hydrogen residing

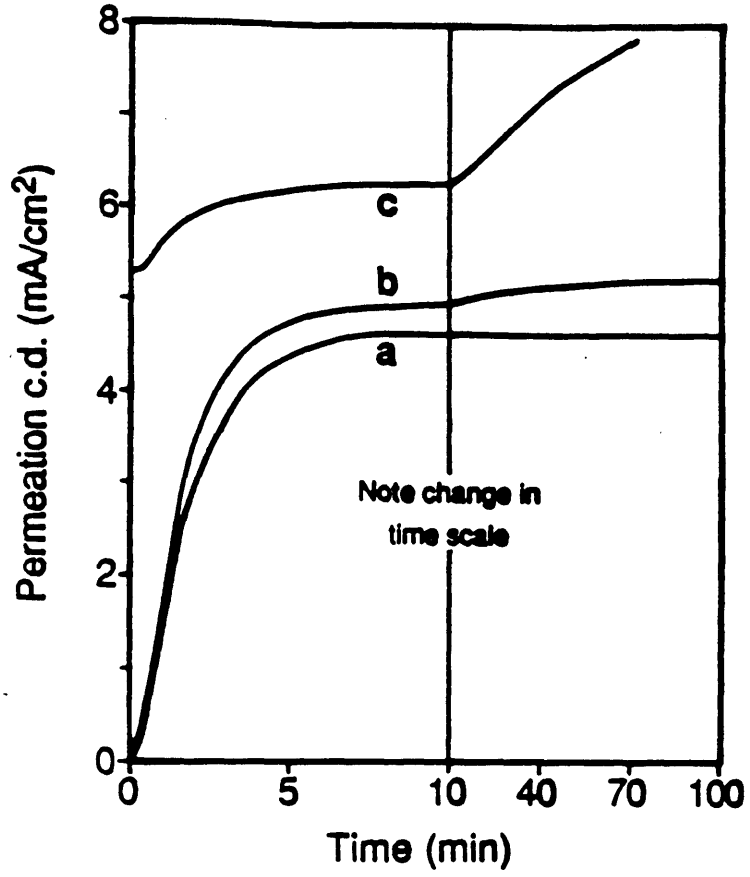

Fig. 39. Hydrogen permeation in palladium specimen 100 μm thick at 28°C. Transients **a** and **b** correspond to cathodic current densities (i_c) of 4.6 and 5.3 mA/cm^2. Transient **c** is produced by stepping i_c from 5.6 to 10 mA/cm^2.

in the specimen did not increase once steady-state permeation was attained, regardless of the length of time permeation was continued. With values of i_c that produced the second type of permeation transient, the quantity of hydrogen extracted was much greater than in the former case, and increased dramatically with continued permeation.

While the temporary reduction in the absorption efficiency encountered with higher values i_c would suggest that hydride is forming (H_2 evolution at the input surface was not observed, so the lost increment of hydrogen flux must be stored within the specimen), the increase in hydrogen content with increasing time of permeation clearly indicates that the second phase, with its much higher hydrogen concentration, has formed. Growth of the hydride layer must cease when the absorption efficiency again reaches 1.00. The state of the specimen in this condition is illustrated in Fig. 40; the concentration gradient across the reduced thickness of α phase, (L - a), corresponds to the flux of hydrogen being introduced at the input surface.

If the transition in permeation behavior is approached with sufficiently small increases of i_c, the value which first produces the apparent reduction in absorption efficiency may be substituted for i_{ss} in equation [4] (see section 5.) to calculate C_o. Values determined in this manner for several palladium foils of differing thicknesses were in agreement with the room-temperature terminal solubility of hydrogen in palladium determined by Simons and Flanagan (69) from pressure-composition isotherms.

The transient in the permeation current produced by an increase in i_c following the formation of a hydride layer (transient **c**, Fig. 39) is most interesting. Since the initial increase in the permeation current is too rapid to correspond to uniform forward motion of the phase boundary, it would appear that certain regions of the α phase transform to hydride more readily than others.

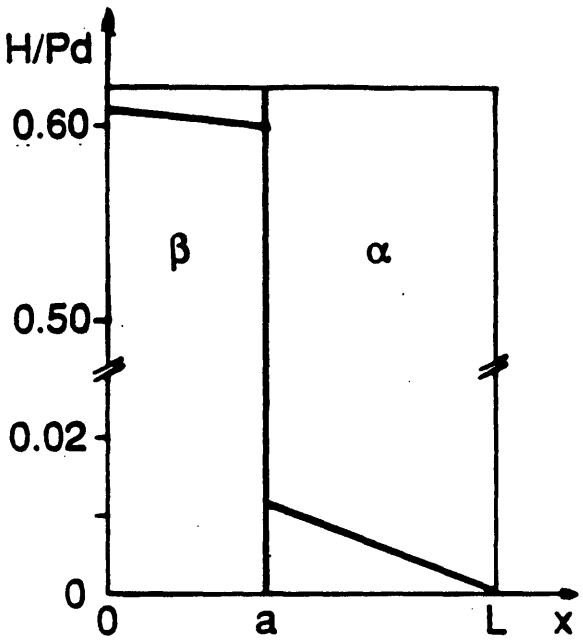

Fig. 40. Steady state concentration gradient in palladium specimen with a layer of hydride at the input surface.

The results described above contrast sharply with those reported by Bowker and Piercy (67). Using palladium foils that were vacuum annealed and then coated with a thin electrodeposit of palladium, they found that i_{ss} became independent of i_c following the formation of hydride on the input surface (Fig. 41). The evolution of H_2 from the input surface was also observed in this regime. These observations suggest that the electroplated input surface favors the hydrogen evolution pathway at higher values of i_c. As a consequence, the growth of the hydride layer into the α phase was significantly retarded. In the present study, etching of the palladium with aqua regia has been shown to provide complete absorption of hydrogen, even in the presence of a thick hydride layer on the input surface. It would appear that this treatment might be useful to those individuals who are presently attempting to reproduce the "cold fusion" phenomenon recently reported by Fleischmann and Pons (70) in palladium deuteride.

Hydride formation on the input surface of an electrodeposited nickel permeation foil has been more difficult to detect. "Plateau" behavior similar to that reported by Bowker and Piercy with palladium is evident in Fig. 36. The detection of a slow rise in the steady-state permeation current indicative of a growing hydride layer was made nearly impossible by the interrelated problems of Joule heating and surface contamination. Increasing the salt concentration to limit the former only increased the accumulation of contaminants that could also produce a slow rise in the permeation current density. Thus, the terminal solubility for hydrogen in nickel has yet to be determined. Nonetheless, it can be stated with certainty that hydride does not form at cathodic current densities less than that at which the permeation current density plateaus; i.e., approximately 50 mA/cm^2.

The use of a palladium coating on nickel specimens has also been investigated. Hydrogen permeation could not be detected when palladium was electrodeposited onto the input surface.

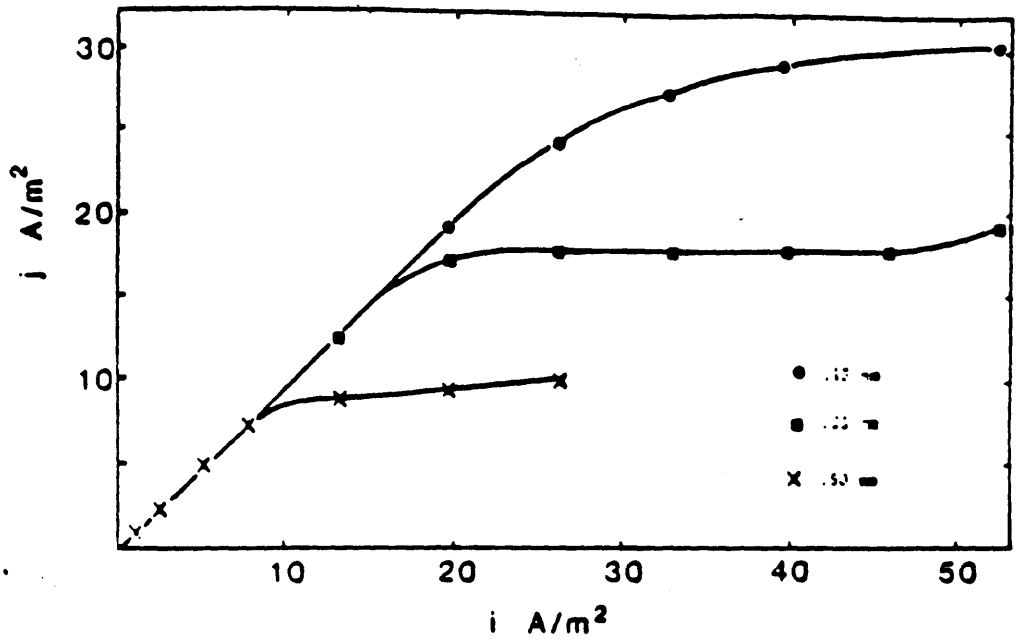

Fig. 41. Relationship between the cathodic current density (i) and the steady state permeation current density (j) for palladium coated with electrodeposited palladium. Three specimens of different thickness. (Ref. 67)

However, when the coated specimen was reversed, the palladium was found to have no adverse effect on the permeation (relative to uncoated specimens). This behavior suggests that hydrogen can be trapped at the Pd-Ni interface when the high-concentration surface is coated. The trap sites appear to be unsaturable, suggesting that they are blisters that form through disbonding of the interface. Thus, the critical issue is the adhesion of the palladium coating to the nickel surface, which is usually covered with an oxide film. Several methods of surface activation (i.e., removing the oxide) prior to electrodeposition did not solve the problem. A similar problem involving tantalum specimens (66) was overcome by preparing the foils in ultrahigh vacuum; the specimen was heated to remove the oxide prior to vapor deposition of the palladium. This approach was not investigated.

10. References

1. D.H. Lassila and H.K. Birnbaum, Acta Metall., **34**, 1237 (1986).
2. R.H. Jones, M.T. Thomas and D.R. Baer, Scripta Metall., **18**, 47 (1984).
3. J.A. Donovan, Met. Trans. A, **7A**, 145 (1976).
4. G.S. Frankel and R.M. Latanision, Met. Trans. A, **17A**, 861 (1986).
5. G.S. Frankel and R.M. Latanision, Met. Trans. A, **17A**, 869 (1986).
6. T. Mutschele and R. Kirchheim, Scripta Metall., **21**, 135 (1987).
7. M.D. Archer and N.C. Grant, Proc. Roy. Soc. Lond., **A395**, 165 (1984).
8. H.E.G. Rommal and P.J. Moran, J. Electrochem. Soc., **135**, 343 (1988).
9. T. Schober and C. Dieker, Met. Trans. A, **14A**, 2440 (1983).
10. D. Tseng, Q.Y. Long and K. Tangri, Scripta Metall., **22**, 649 (1988).
11. T.M. Harris and R.M. Latanision, accepted for publication in Scripta Metall. (1989).
12. T. Tsuru and R.M. Latanision, Scripta Metall., **16**, 575 (1982).
13. B. Ladna and H.K. Birnbaum, Acta Metall., **35**, 2537 (1987).
14. R.W. Balluffi, Met. Trans. A, **13A**, 2069 (1982).
15. V.M. von Stackelberg and P. Ludwig, Z. Naturforsch., **19a**, 93 (1964).
16. A. Kimura and H.K. Birnbaum, Scripta Metall., **21**, 219 (1987).
17. A. Kimura and H.K. Birnbaum, Acta Metall., **36**, 757 (1988).
18. J. Yao and J.R. Cahoon, Scripta Metall., **22**, 1817 (1988).
19. G. Herrmann, H. Gleiter and G. Baro, Acta Metall., **24**, 353 (1976).
20. W.M. Robertson, Z. Metallkde., **64**, 436 (1973).
21. M.R. Louthan, J.A. Donovan and G.R. Caskey, Jr., Acta Metall., **23**, 745 (1975).
22. R.-W. Lin and H.H. Johnson, Scripta Metall., **16**, 1091 (1982).
23. F. Fukushima and H.K. Birnbaum, Acta Metall., **32**, 851 (1984).
24. S.W. Stafford and R.B. McLellan, Acta Metall., **22**, 1463 (1974).

25. S.-M. Lee and J.-Y. Lee, Met. Trans. A, **17A**, 181 (1986).

26. R.M. Latanision and H. Operhauser, Jr., Met. Trans., **5**, 483 (1974).

27. M.I. Baskes and V. Vitek, Met. Trans. A, **16A**, 1625 (1985).

28. J.O'M. Bockris, M.A. Genshaw and M.A. Fullenwider, Electrochim. Acta, **15**, 47 (1970).

29. A. Atrens, D. Mezzanotte, N.F. Fiore and M.A. Genshaw, Corr. Sci., **20**, 673 (1980).

30. R.M. Latanision and M. Kurkela, Corrosion, **39**, 174 (1983).

31. J.O'M. Bockris and P.K. Subramanyan, Acta Metall., **19**, 1205 (1971).

32. A. McNabb and P.K. Foster, Trans. TMS-AIME, **227**, 618 (1963).

33. A.W. Thompson and H.J. Saxton, Met. Trans., **4**, 1599 (1973).

34. D.A. Fanner and R.A.F. Hammond, Trans. Inst. Met. Fin., **36**, 32 (1958/59).

35. G.F. Vander Voort, "Metallography", McGraw-Hill, NY, 1984, 86.

36. B. MacDougall and M. Cohen, J. Electrochem. Soc., **123**, 191 (1976).

37. M.A.V. Devanathan and Z. Stachurski, Proc. Royal Soc., **A270**, 90 (1962).

38. R.M. Barrer, Trans. Faraday Soc. A, **97**, 286 (1939).

39. G.F. Vander Voort, "Metallography", McGraw-Hill, NY, 1984, 447.

40. B. O'Sullivan, Trans. Faraday Soc., **26**, 89 (1930).

41. A. Brenner, V. Zentner and C.W. Jennings, Plating, **39**, 865 (1952).

42. E.J. Suoninen and T. Hakkarainen, J. Mat. Sci., **3**, 446 (1968).

43. R. Weil, W.N. Jacobus, Jr. and S.J. DeMay, J. Electrochem. Soc., **111**,1046 (1964).

44. J. McBreen, L. Nanis and W. Beck, J. Electrochem. Soc., **113**, 1218 (1966).

45. S.K. Yen and H.C. Shih, J. Electrochem. Soc., **135**, 1169 (1988).

46. P.H. Pumphrey, Scripta Metall., **14**, 695 (1980).

47. M.A.V. Devanathan and Z. Stachurski, J. Electrochem. Soc., **111**, 619 (1964).

48. A. Kimura and H.K. Birnbaum, Acta Metall., **35**, 1077 (1987).

49. E.W. Hart, Acta Metall., **5**, 597 (1957).

50. P.G. Shewmon, "Diffusion in Solids", J. Williams Book Co., Jenks, OK, 1983, 47.

51. C.S. Smith and L. Guttman, Trans. AIME, **197**, 81 (1953).

52. T. Mutschele and R. Kirchheim, Scripta Metall., **21**, 1101 (1987).

53. L.G. Harrison, Trans, Faraday Soc., **57**, 1191 (1961).

54. D. Gupta, D.R. Campbell and P.S. Ho in "Thin Films-Interdifusion and Reactions", J.M. Poate, K.N. Tu and J.W. Mayer, Eds., Wiley, NY, 1978, 161.

55. D. R. Campbell, Bull. Amer. Phys. Soc., **19**, 347 (1974).

56. C. Zener in "Imperfections in Nearly Perfect Crystals", W. Shockley, Ed., Wiley, New York, 1952, 289.

57. H.H. Johnson, N. Quick and A.J. Kumnick, **13**, 67 (1979).

58. A.J. Kumnick and H.H. Johnson, Acta Metall., **28**, 33 (1980).

59. W.M. Robertson, Met. Trans A, **10 A**, 489 (1979).

60. A.W. Thompson and B.A. Wilcox, Scripta Metall., **6**, 689 (1972).

61. E. Vafaei-Makhsoos, E.D. Thomas and L.E. Toth, Met. Trans. A, **9A**, 1449 (1978).

62. S.M. Bruemmer, R.H. Jones, M.T. Thomas and D.R. Baer, Met. Trans. A, **14A**, 223 (1983).

63. J.-P. Hirvonen, J.W. Mayer and H.H. Johnson, Scripta Metall., **23**, 263 (1989).

64. C.R.M. Grovenor, H.T.G. Hentzell and D.A. Smith, Acta Metall., **32**, 773 (1984).

65. A.J. Kumnick and H.H. Johnson, Met. Trans. A, **6A**, 1087 (1975).

66. N. Boes and H. Zuchner, Z. Naturforsch., **31a**, 760 (1976).

67. J. Bowker and G.R. Piercy, Met. Trans. A, **16A**, 715 (1985).

68. J.G. Early, Acta Metall., **26**, 1215 (1978).

69. J.W. Simons and T. Flanagan, J. Phys. Chem., **69**, 3773 (1965).

70. M. Fleischmann and S. Pons, J. Electroanal. Chem., **261**, 301 (1989).